

Supporting Information

Isomerism, Aggregation-Induced Emission and Mechanochromism of Isocyanide Cycloplatinated(II) Complexes

Mónica Martínez-Junquera, Rebeca Lara, Elena Lalinde and M. Teresa Moreno**

^a Departamento de Química-Centro de Síntesis Química de La Rioja, (CISQ),
Universidad de La Rioja, 26006, Logroño, Spain. E-mail: teresa.moreno@unirioja.es

| Contents: | Page |
|--|-------------|
| 1.- Computational Data relative to stability of 4-<i>trans/cis</i> and 6-<i>trans/cis</i> | S2 |
| 2.- Characterization of Complexes | S4 |
| 2.1.- NMR Spectra | S5 |
| 2.2 Crystal Structures | S9 |
| 3.- Photophysical Properties | S15 |
| 4.- DFT and TD-DFT Calculations | S24 |

1.- Computational Data relative to stability of 4-*trans*/*cis* and 6-*trans*/*cis*

Table S1. DFT optimized geometries for ground state of compounds **4-*trans*** and **6-*cis*** and their respective isomers **4-*cis*** and **6-*trans*** in CH₂Cl₂.

| | 4 | 4-<i>trans</i> | 4-<i>cis</i> |
|------------------|-----------|-----------------------|---------------------|
| | X-ray | S ₀ | S ₀ |
| Pt(1)-N(2) | 2.049(5) | 2.110 | 2.134 |
| Pt(1)-C(10) | 2.049(5) | 2.062 | 2.041 |
| Pt(1)-C(1) | 1.933(6) | 1.900 | 2.010 |
| Pt(1)-C(21) | 2.087(7) | 2.054 | 1.970 |
| N(1)-C(1) | 1.156(7) | 1.172 | 1.173 |
| C(21)-C(22) | 1.058(8) | 1.229 | 1.226 |
| N(2)-Pt(1)-C(10) | 80.58(19) | 79.63 | 79.77 |
| C(1)-Pt(1)-C(21) | 89.1(2) | 90.72 | 88.60 |
| N(2)-Pt(1)-C(21) | 93.4(2) | 94.12 | - |
| C(1)-Pt(1)-C(10) | 97.1(2) | 95.54 | - |
| N(2)-Pt(1)-C(1) | - | - | 98.11 |
| C(1)-Pt(1)-C(21) | - | - | 93.53 |

| | 6 | 6-<i>trans</i> | 6-<i>cis</i> |
|----------------|------------|-----------------------|---------------------|
| | X-ray | S ₀ | S ₀ |
| Pt(1)-N(1) | 2.102(3) | 2.181 | 2.184 |
| Pt(1)-C(1) | 2.016(4) | 2.052 | 2.037 |
| Pt(1)-C(16) | 1.960(4) | 1.893 | 2.017 |
| Pt(1)-C(25) | 1.977(4) | 2.067 | 1.968 |
| N(2)-C(16) | 1.178(5) | 1.171 | 1.173 |
| C(25)-C(26) | 1.186(5) | 1.229 | 1.226 |
| C(1)-Pt-N(1) | 79.92(14) | 79.15 | 79.23 |
| C(16)-Pt-C(25) | 84.39(15) | 85.55 | 85.34 |
| C(16)-Pt-N(1) | 101.57(13) | - | 102.92 |
| C(25)-Pt-C(1) | 93.62(15) | - | 92.30 |
| C(25)-Pt-N(1) | - | 101.12 | - |
| C(16)-Pt-C(1) | - | 94.08 | - |

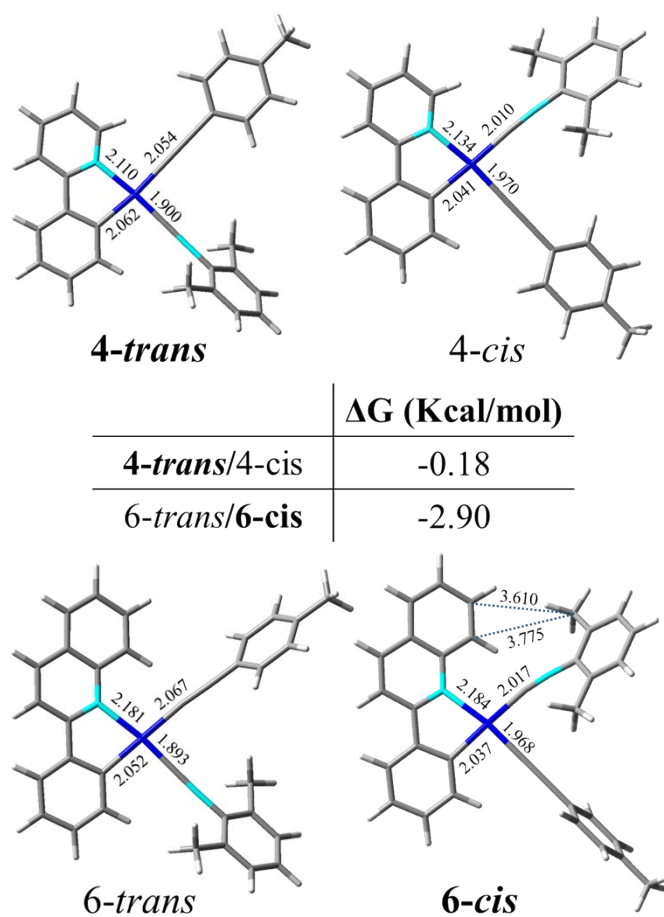


Figure S1. Optimized geometries by DFT calculations for compounds **4**, **6** (*trans* and *cis*) and their respective isomers **4-cis** and **6-trans** with the differences in the ground state energies between the *cis* and the *trans* isomers (bond lengths in Å).

2.- Characterization of complexes

Complexes **1-3** exhibit in their IR spectra a strong characteristic band at 2179-2188 cm^{-1} , assigned to the $\nu_{\text{C}\equiv\text{N}}$ stretching mode, shifted to higher frequencies with respect to the free CNXyl ligand (2131 cm^{-1}), whereas the alkynyl isocyanide complexes **4-6** show two close stretching bands, one corresponding to the $\nu_{\text{C}\equiv\text{N}}$ (2153-2179 cm^{-1}), slightly shifted to lower frequencies in relation to the corresponding precursor, and the other to the $\nu_{(\text{C}=\text{C})}$ alkynyl stretching mode (2105-2121 cm^{-1}). The ESI(+) mass spectra of **1-3** display the molecular peaks associated with $[\text{M}-\text{Cl}]^+$ molecular ions, whereas **4-6** show peaks related to $[\text{M}+\text{Na}]^+$ or $[\text{M}+\text{H}]^+$, and some associated with the loss of the $\text{C}\equiv\text{CTol}$ group.

In the ^1H and $^{13}\text{C}\{^1\text{H}\}$ NMR, chloro-isocyanide complexes show only the signals corresponding to one cyclometalated and to one isocyanide ligand, in agreement with the presence of only one isomer (see Experimental Section and Figures S2-S5). Notably, the most deshielded ^1H NMR signal, which appears as a doublet in **1** and **2** with platinum satellites ($^3J_{\text{Pt-H}} \sim 29$ Hz), is attributed to H^2 and to H^8 in **3**. In **1** and **2**, the carbon resonance of C^{12} is visible with a coupling constant of 1014 (**1**), 1042 Hz (**2**), in the same order than for *cis*-[Pt(ppy) $_2$] (1147 Hz) (*Inorg. Chem.*, 1984, **23**, 4249). The methyl groups of the CNXyl appear as a singlet at 2.58-2.69 ppm in the proton and at ~ 19 ppm in the $^{13}\text{C}\{^1\text{H}\}$ NMR. The NMR spectroscopic investigations indicate that, in solution, the phenylquinoliny-based complexes **4** and **5** maintain the *trans-N,CNXyl* geometry. The substitution of the chloride by the $\text{C}\equiv\text{CTol}$ group produces a downfield shift of the most deshielded proton (δH^2 9.83 **4** vs 9.68 **1**; 9.92 **5** vs 9.64 **2**) and to a lesser extent also to the H^{11} signal (δH^{11} 7.86 **4** vs 7.75 **1**; 7.38 **5** vs 7.18 **2**) (Figures S2, S3). The Me of the Tol and Xyl groups appear at ~ 2.30 and 2.60 ppm, respectively in the ^1H NMR and at ~ 21 and 19 ppm in the $^{13}\text{C}\{^1\text{H}\}$. In accordance with the structure, the NOESY spectrum of **4** confirms a NOE effect (cross signal marked in circle, Figure S4) between $\text{H}^{11}_{\text{ppy}}$ and the CH_3 of the CNXyl ligand, due to the proximity of these protons. For the pq-alkynyl complex **6**, the substitution of Cl by $\text{C}\equiv\text{CTol}$ and inversion of the configuration in relation to the precursor **3** is reflected in an upfield shift for the H^8 signal (δH^8 8.84 **6** vs 9.82 **3**) and a clear downfield shift for the *ortho* proton H^{12} (δH^{12} 8.57 **6** vs 7.78 **3**) (Figure S5).

2.1- NMR Spectra

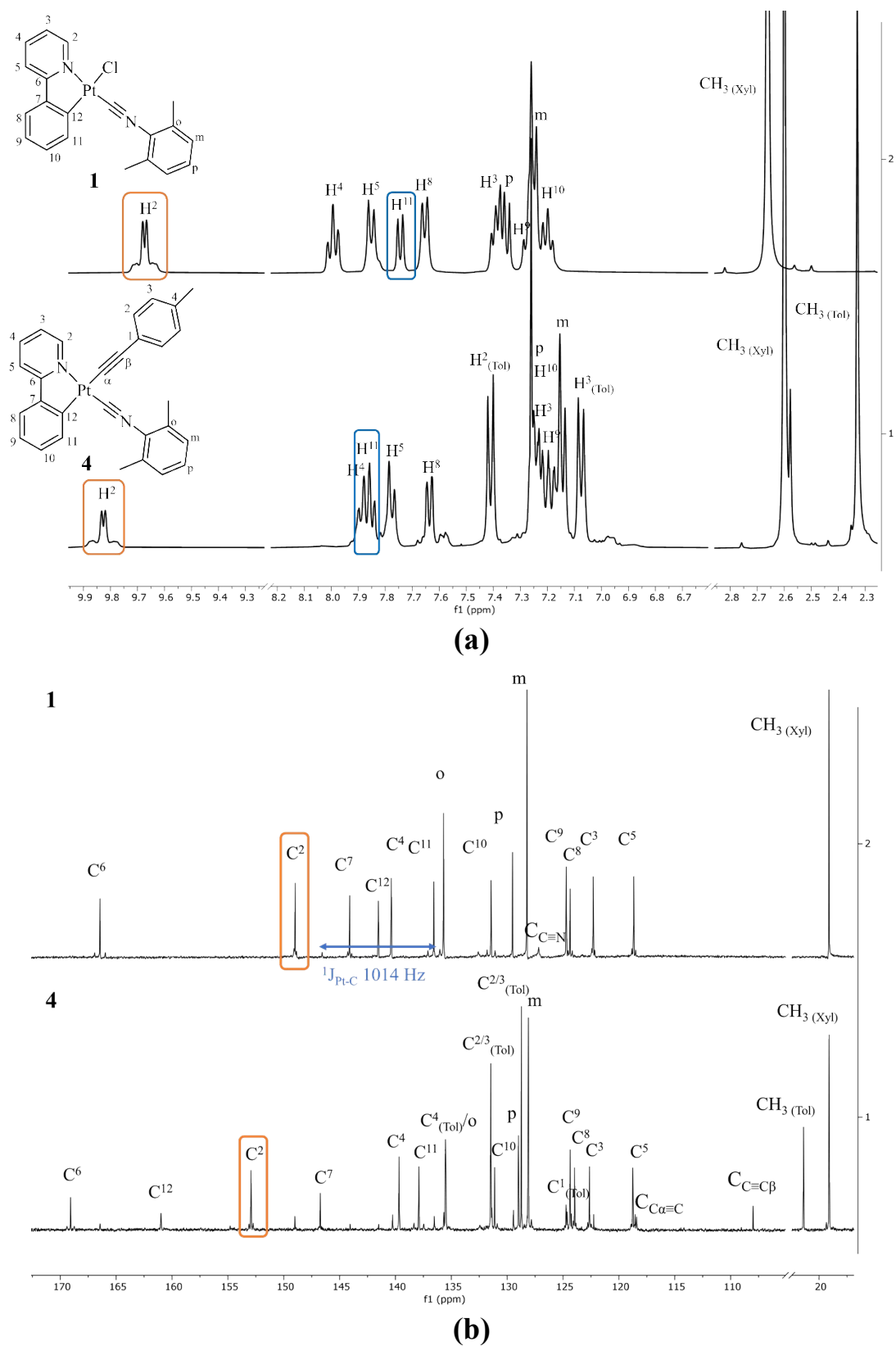
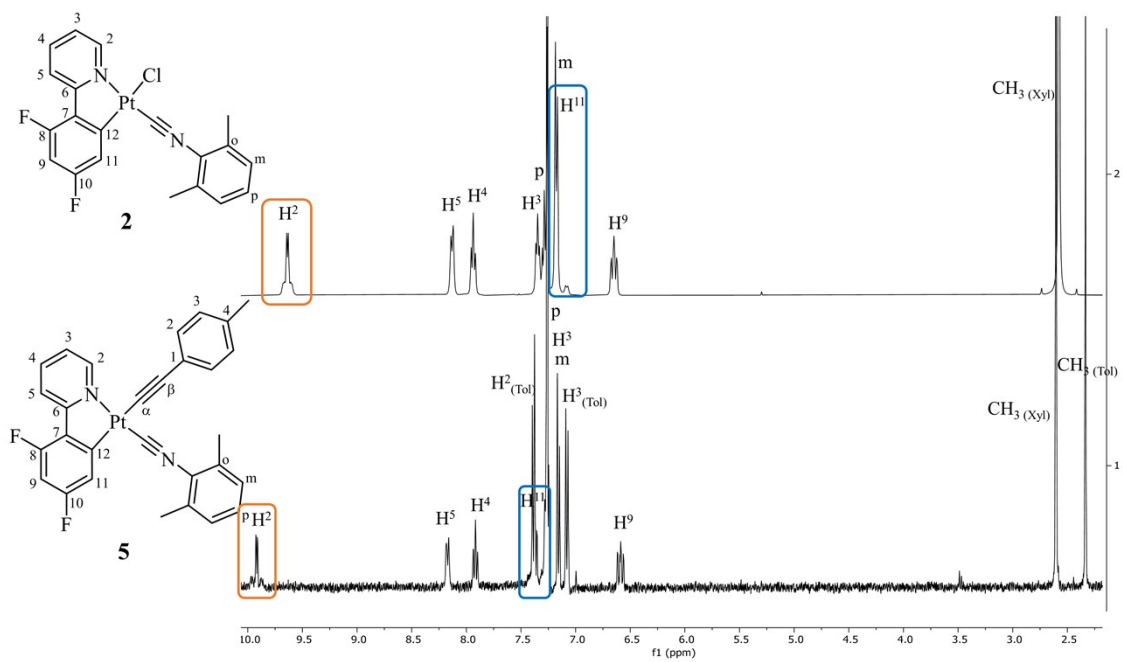
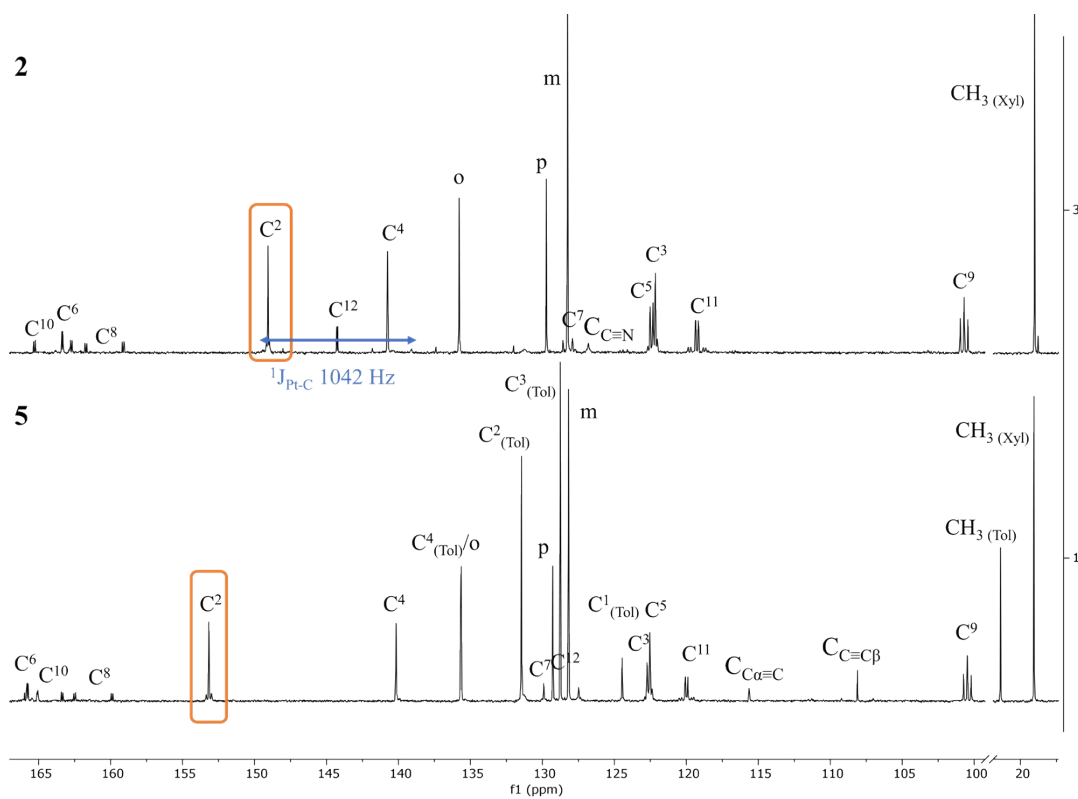


Figure S2. NMR spectra of **1** and **4** in CDCl_3 at 298 K (a) ^1H , (b) $^{13}\text{C}\{^1\text{H}\}$.

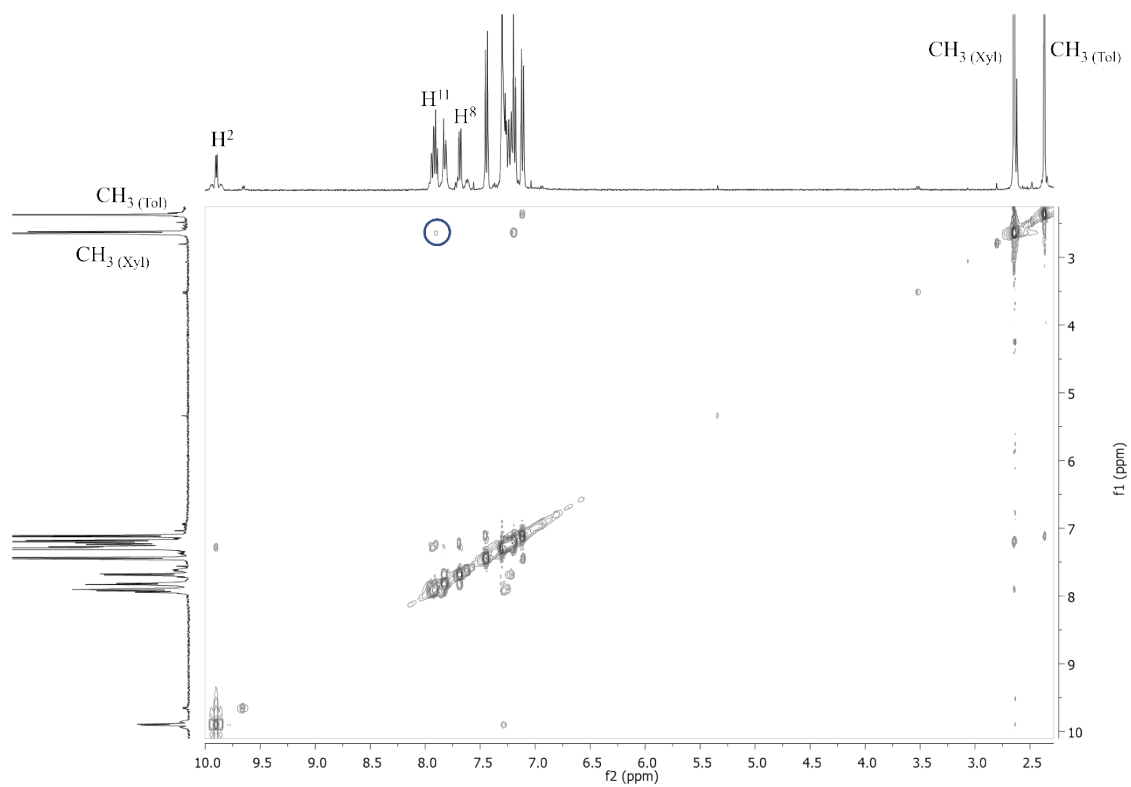


(a)

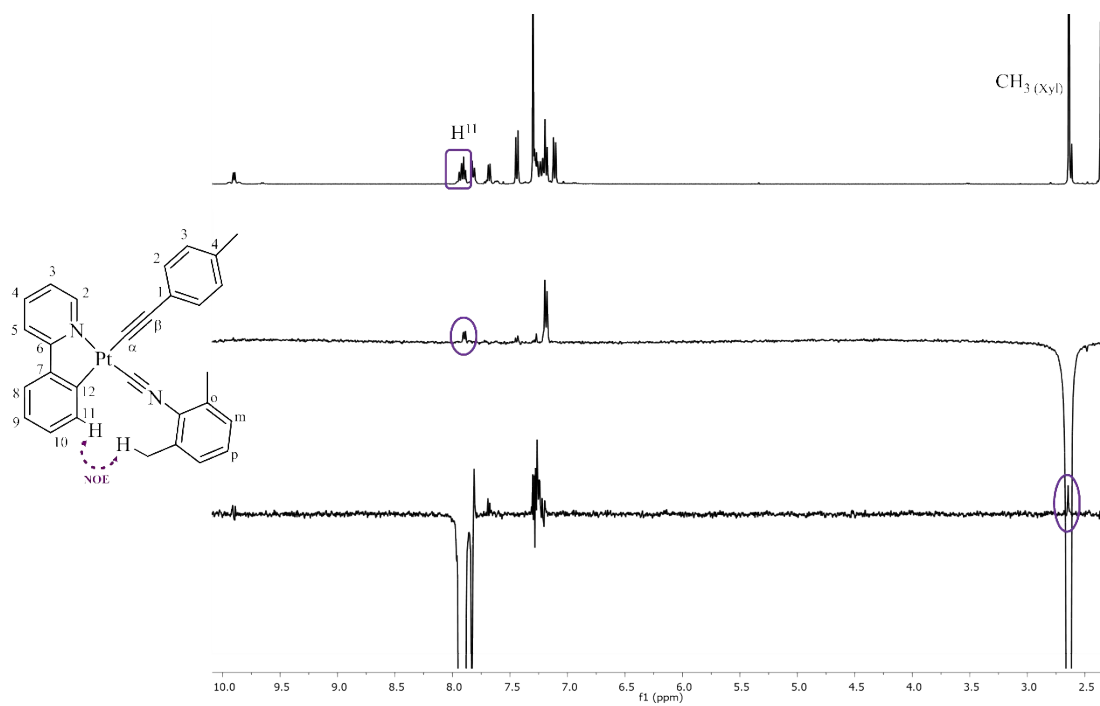


(b)

Figure S3. NMR spectra of **2** and **5** in CDCl_3 at 298 K (a) ^1H , (b) $^{13}\text{C}\{^1\text{H}\}$.

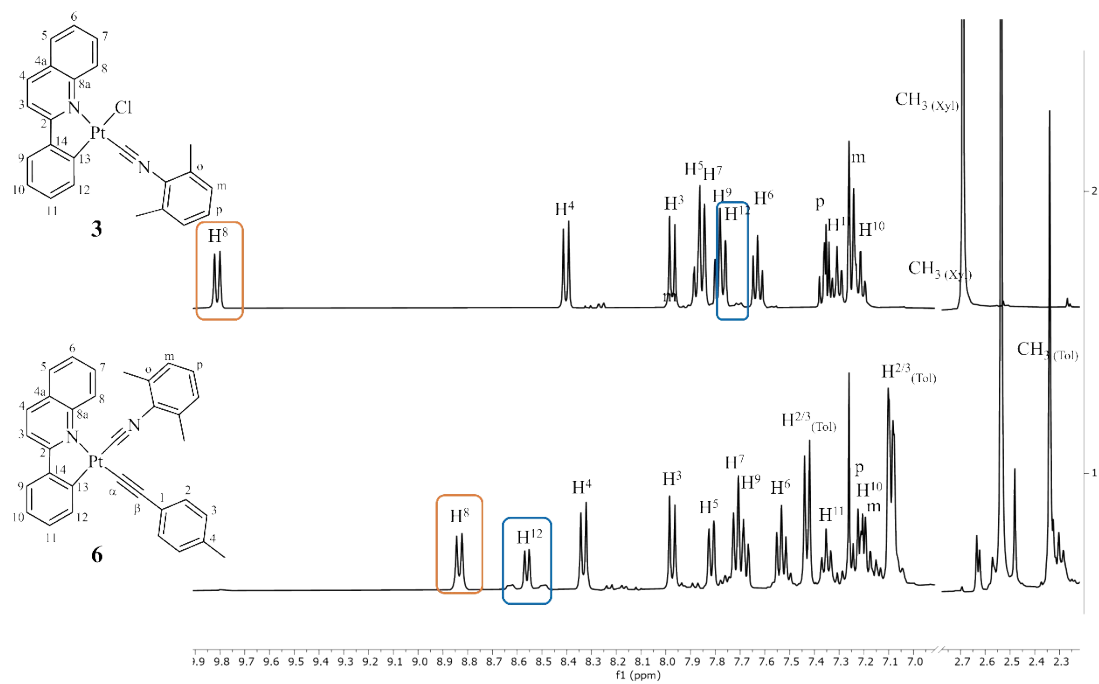


(a)

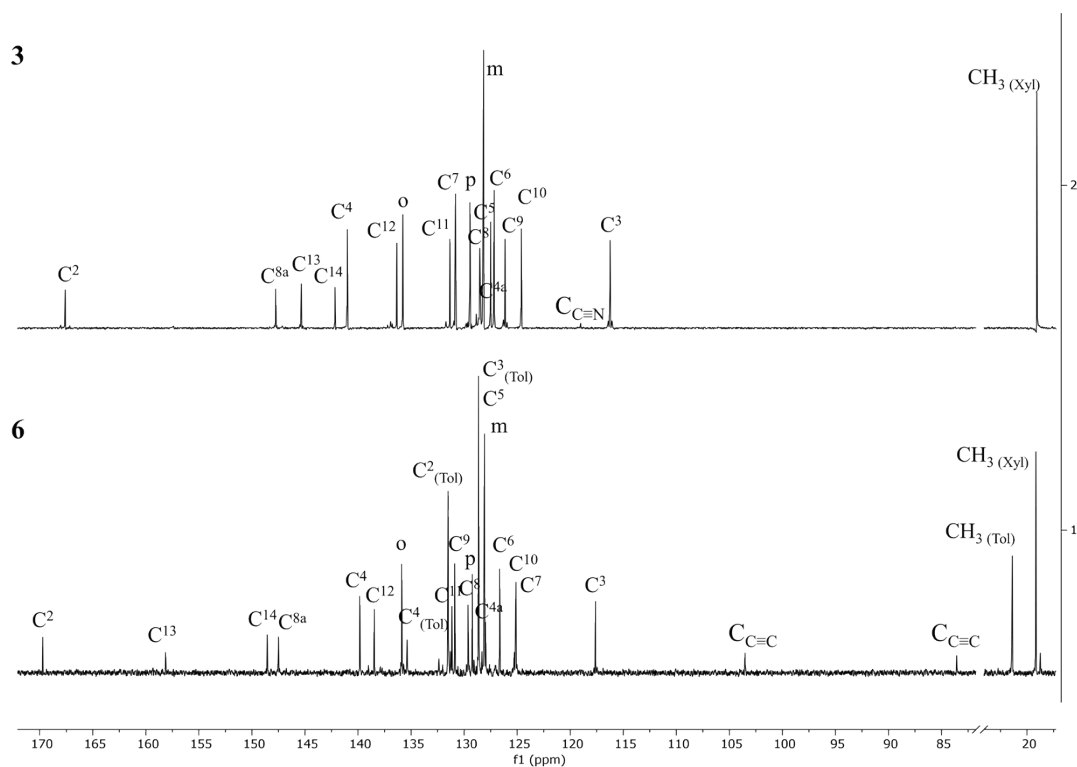


(b)

Figure S4. (a) NOESY and (b) NOEs with selective irradiation to 2.60 (CH₃, Xyl) and 7.86 (H¹¹) ppm of **4** in CDCl₃ at 298 K.



(a)



(b)

Figure S5. NMR spectra of **3** and **6** in CDCl_3 at 298 K, (a) ^1H , (b) $^{13}\text{C}\{^1\text{H}\}$.

2.2 Crystal Structures

Table S2. Selected distances (Å) and angles (°) for complexes **1**, **3**, **4**, **5**·CHCl₃ and **6**

| 1 | | | |
|---------------------------|------------|-------------------|------------|
| Distances (Å) | | Angles (°) | |
| Pt(1)-N(2) | 2.063(3) | C(10)-Pt(1)-N(2) | 80.62(15) |
| Pt(1)-C(10) | 1.986(4) | C(1)-Pt(1)-Cl(1) | 89.43(12) |
| Pt(1)-C(1) | 1.901(4) | N(2)-Pt(1)-Cl(1) | 94.55(10) |
| Pt(1)-Cl(1) | 2.3901(10) | C(1)-Pt(1)-C(10) | 95.47(17) |
| N(1)-C(1) | 1.153(5) | N(1)-C(1)-Pt(1) | 177.5(4) |
| N(1)-C(2) | 1.399(5) | C(1)-N(1)-C(2) | 173.5(4) |
| C(15)-C(16) | 1.465(5) | | |
| 3 | | | |
| Distances (Å) | | Angles (°) | |
| Pt(1)-N(1) | 2.096(3) | C(1)-Pt(1)-N(1) | 80.75(15) |
| Pt(1)-C(1) | 1.993(4) | C(16)-Pt(1)-Cl(1) | 84.54(11) |
| Pt(1)-C(16) | 1.884(4) | N(1)-Pt(1)-Cl(1) | 100.50(9) |
| Pt(1)-Cl(1) | 2.4097(9) | C(16)-Pt(1)-C(1) | 94.34(16) |
| N(2)-C(16) | 1.161(5) | C(16)-N(2)-C(17) | 171.4(4) |
| N(2)-C(17) | 1.397(5) | N(2)-C(16)-Pt(1) | 176.6(4) |
| C(6)-C(7) | 1.460(6) | C(16)-Pt(1)-N(1) | 174.96(13) |
| 4 | | | |
| Distances (Å) | | Angles (°) | |
| Pt(1)-N(2) | 2.049(5) | N(2)-Pt(1)-C(10) | 80.58(19) |
| Pt(1)-C(10) | 2.049(5) | C(1)-Pt(1)-C(21) | 89.1(2) |
| Pt(1)-C(1) | 1.933(6) | N(2)-Pt(1)-C(21) | 93.4(2) |
| Pt(1)-C(21) | 2.087(7) | C(1)-Pt(1)-C(10) | 97.1(2) |
| N(1)-C(1) | 1.156(7) | N(1)-C(1)-Pt(1) | 177.2(5) |
| C(21)-C(22) | 1.058(8) | C(22)-C(21)-Pt(1) | 170.5(6) |
| N(1)-C(2) | 1.392(6) | C(1)-N(1)-C(2) | 176.0(7) |
| | | C(21)-C(22)-C(23) | 173.7(5) |
| 5·CHCl₃ | | | |
| Distances (Å) | | Angles (°) | |
| Pt(1)-N(1) | 2.062(3) | C(11)-Pt(1)-N(1) | 80.18(15) |
| Pt(1)-C(11) | 2.026(4) | C(12)-Pt(1)-C(21) | 89.44(17) |
| Pt(1)-C(12) | 1.877(4) | C(21)-Pt(1)-N(1) | 95.32(15) |
| Pt(1)-C(21) | 2.039(4) | C(12)-Pt(1)-C(11) | 95.17(17) |
| N(2)-C(12) | 1.169(5) | N(2)-C(12)-Pt(1) | 178.5(4) |
| C(21)-C(22) | 1.203(6) | C(22)-C(21)-Pt(1) | 175.8(4) |
| | | C(12)-N(2)-C(13) | 178.6(5) |
| | | C(21)-C(22)-C(23) | 168.5(4) |

| 6 | | | |
|----------------------|----------|-------------------|------------|
| Distances (Å) | | Angles (°) | |
| Pt(1)-N(1) | 2.102(3) | C(1)-Pt-N(1) | 79.92(14) |
| Pt(1)-C(1) | 2.016(4) | C(16)-Pt-C(25) | 84.39(15) |
| Pt(1)-C(16) | 1.960(4) | C(16)-Pt-N(1) | 101.57(13) |
| Pt(1)-C(25) | 1.977(4) | C(25)-Pt-C(1) | 93.62(15) |
| N(2)-C(16) | 1.178(5) | N(2)-C(16)-Pt | 169.6(3) |
| C(25)-C(26) | 1.186(5) | C(26)-C(25)-Pt | 173.4(3) |
| N(2)-C(17) | 1.416(5) | C(16)-N(2)-C(17) | 175.1(4) |
| C(27)-C(26) | 1.446(5) | C(25)-C(26)-C(27) | 172.9(4) |

Table S3. X-ray Crystallographic Data for **1** and **3**.

| | 1 | 3 |
|--|--|--|
| Empirical formula | C ₂₀ H ₁₇ Cl N ₂ Pt | C ₂₆ H ₁₉ Cl N ₂ Pt |
| F_w | 515.90 | 589.97 |
| T (K) | 173(1) | 193(1) |
| Wavelength (Å) | 0.71073 | 0.71073 |
| Crystal system | Monoclinic | Monoclinic |
| Space group | P 21/c | P 21/c |
| Crystal size (mm³) | 0.2 x 0.1 x 0.05 | 0.3 x 0.1 x 0.05 |
| a (Å) | 9.2450(2) | 17.2404(7) |
| b (Å) | 10.1560(5) | 6.32300(10) |
| c (Å) | 19.1660(9) | 19.4207(8) |
| α (°) | 90 | 90 |
| β (°) | 96.871(2) | 110.9280(10) |
| γ (°) | 90 | 90 |
| V (Å³) | 1786.61(13) | 1977.41(12) |
| Z | 4 | 4 |
| D_{calcd} (Mg/m³) | 1.918 | 1.982 |
| Absorption coefficient (mm⁻¹) | 8.006 | 7.247 |
| F(000) | 984 | 1136 |
| θ range for data collection (deg) | 2.991 to 26.021 | 3.497 to 27.468 |
| Index ranges | -11 ≤ h ≤ 11, -12 ≤ k ≤ 12, -23 ≤ l ≤ 23 | -22 ≤ h ≤ 22, -8 ≤ k ≤ 8, -25 ≤ l ≤ 25 |
| Reflections collected | 20293 | 29154 |
| Independent reflections | 3514 [R(int) = 0.0481] | 4501 [R(int) = 0.0512] |
| Data / restraints/ parameters | 3514 / 0 / 217 | 4501 / 0 / 253 |
| Goodness-of-fit on F² ^a | 1.057 | 1.047 |
| Final R index | R ₁ = 0.0265 | R ₁ = 0.0260 |
| [I > 2σ(I)]^a | wR ₂ = 0.0655 | wR ₂ = 0.0628 |
| R indexes (all data)^a | R ₁ = 0.0331, wR ₂ = 0.0691 | R ₁ = 0.0341, wR ₂ = 0.0662 |
| Largest diff. peak and hole (e. Å⁻³) | 1.791 and -1.623 | 0.946 and -1.890 |

^a R₁ = $\sum(|F_o| - |F_c|) / \sum|F_o|$; wR₂ = $[\sum w(F_o^2 - F_c^2)^2 / \sum wF_o^2]^{1/2}$; goodness of fit = $\{\sum[w(F_o^2 - F_c^2)^2] / (N_{obs} - N_{param})\}^{1/2}$; w = $[\sigma^2(F_o) + (g_1P)^2 + g_2P]^{-1}$; P = $[\max(F_o^2; 0 + 2F_c^2) / 3]$.

Table S4. X-ray Crystallographic Data for **4**, **5**·CHCl₃ and **6**.

| | 4 | 5 ·CHCl ₃ | 6 |
|--|---|--|---|
| Empirical formula | C ₂₉ H ₂₄ N ₂ Pt | C ₃₀ H ₂₃ Cl ₃ F ₂ N ₂ Pt | C ₃₃ H ₂₆ N ₂ Pt |
| F_w | 595.59 | 750.94 | 645.65 |
| T (K) | 173(1) | 140(2) | 293(1) |
| Wavelength (Å) | 0.71073 | 0.71076 | 0.71073 |
| Crystal system | Monoclinic | Triclinic | Monoclinic |
| Space group | P 21/c | P -1 | P 21/c |
| Crystal size (mm³) | 0.2 x 0.15 x 0.1 | 0.11 x 0.06 x 0.03 | 0.4 x 0.2 x 0.1 |
| a (Å) | 9.6548(2) | 9.138(2) | 12.7065(4) |
| b (Å) | 16.0315(7) | 10.989(3) | 10.8640(3) |
| c (Å) | 15.0237(6) | 14.906(4) | 18.6362(6) |
| α (°) | 90 | 69.314(11) | 90 |
| β (°) | 99.852(2) | 88.231(11) | 93.2650(10) |
| γ (°) | 90 | 78.638(11) | 90 |
| V (Å³) | 2291.09(14) | 1371.6(6) | 2568.43(14) |
| Z | 4 | 2 | 4 |
| D_{calcd} (Mg/m³) | 1.727 | 1.818 | 1.670 |
| Absorption coefficient (mm⁻¹) | 6.143 | 5.444 | 5.487 |
| F(000) | 1160 | 728 | 1264 |
| θ range for data collection (deg) | 2.736 to 25.345 | 2.884 to 27.949 | 2.171 to 26.371 |
| Index ranges | -12 ≤ h ≤ 12, -20 ≤ k ≤ 20, -19 ≤ l ≤ 19 | -12 ≤ h ≤ 12, -14 ≤ k ≤ 14, -19 ≤ l ≤ 19 | -15 ≤ h ≤ 15, -13 ≤ k ≤ 13, -22 ≤ l ≤ 23 |
| Reflections collected | 26530 | 76792 | 32010 |
| Independent reflections | 4156 [R(int) = 0.0484] | 6547 [R(int) = 0.0806] | 5249 [R(int) = 0.0567] |
| Data / restraints / parameters | 4156 / 0 / 283 | 6547 / 0 / 343 | 5249 / 0 / 325 |
| Goodness-of-fit on F² ^a | 1.093 | 1.047 | 1.045 |
| Final R index [I > 2σ(I)]^a | R ₁ = 0.0292 wR ₂ = 0.0671 | R ₁ = 0.0298 wR ₂ = 0.0717 | R ₁ = 0.0249 wR ₂ = 0.0617 |
| R indexes (all data)^a | R ₁ = 0.0389, wR ₂ = 0.0707 | R ₁ = 0.0406, wR ₂ = 0.0759 | R ₁ = 0.0325, wR ₂ = 0.0648 |
| Largest diff. peak and hole (e. Å⁻³) | 1.233 and -1.158 | 0.956 and -1.239 | 1.499 and -1.055 |

^a R₁ = $\sum(|F_o| - |F_c|) / \sum|F_o|$; wR₂ = $[\sum w(F_o^2 - F_c^2)^2 / \sum wF_o^2]^{1/2}$; goodness of fit = $\{\sum[w(F_o^2 - F_c^2)^2] / (N_{obs} - N_{param})\}^{1/2}$; w = $[\sigma^2(F_o) + (g_1P)^2 + g_2P]^{-1}$; P = $[\max(F_o^2; 0 + 2F_c^2)]/3$.

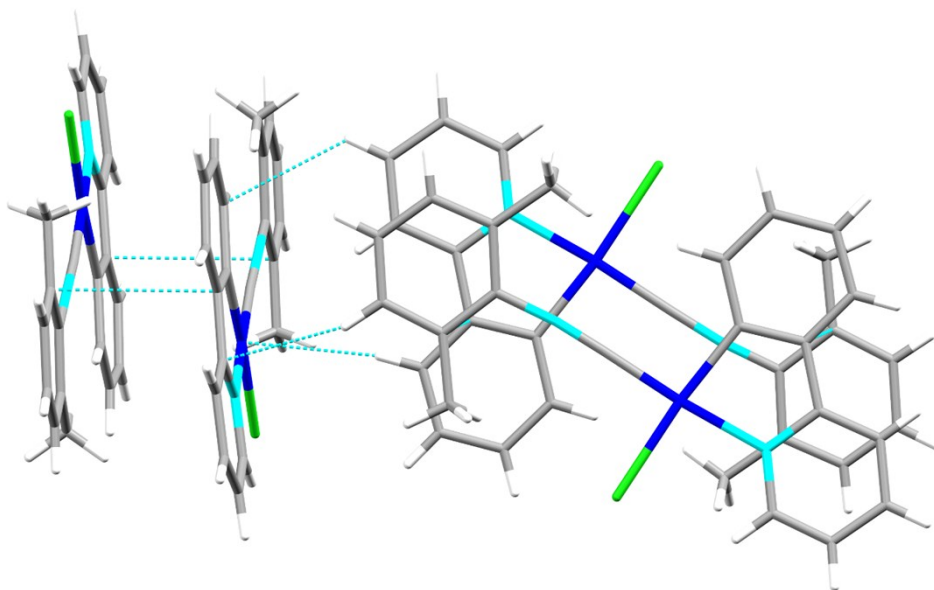


Figure S6. Crystal packing of complex **1** showing head-to-tail pairs of molecules supported by weak intermolecular $\pi \cdots \pi$ interactions (ppy-Xyl 3.48 Å), that connect with other dimers through weak Pt \cdots H (3.0 Å) and C-H \cdots π contacts (C \cdots H 2.78 – 3.01 Å).

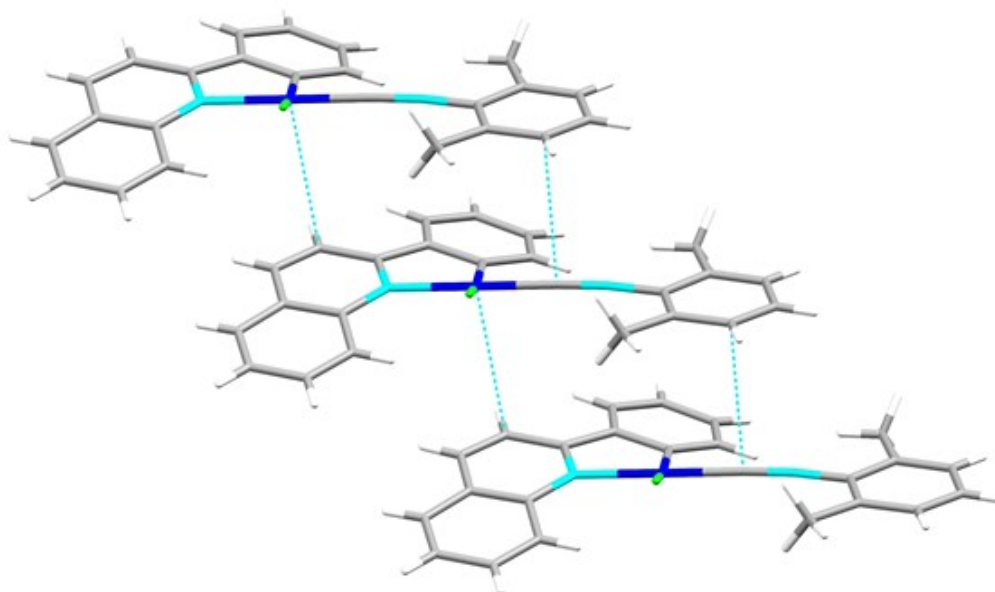


Figure S7. Crystal packing of complex **3** showing head-to-head stacking of molecules in a columnar way along the *b*-axis through secondary weak interactions (C_(xyl) \cdots C \equiv N 3.47 Å, Pt \cdots C_(pq) 3.50 Å).

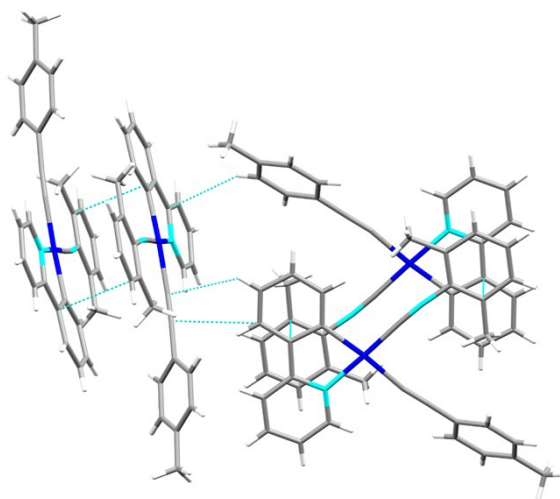


Figure S8. Crystal packing of **4** showing head-to-tail pairs of molecules supported by intermolecular $\pi \cdots \pi$ interactions (ppy-Xyl, 3.55 Å). The interactions between dimers are supported by weak intermolecular contacts $C_{(\text{ppy})} \cdots C_{(\text{C}=\text{C})}$ (3.48 Å), $H_{(\text{ppy})} \cdots C_{(\text{C}=\text{C})}$ (2.86 Å) and $C \cdots H$ (2.88 – 3.04 Å).

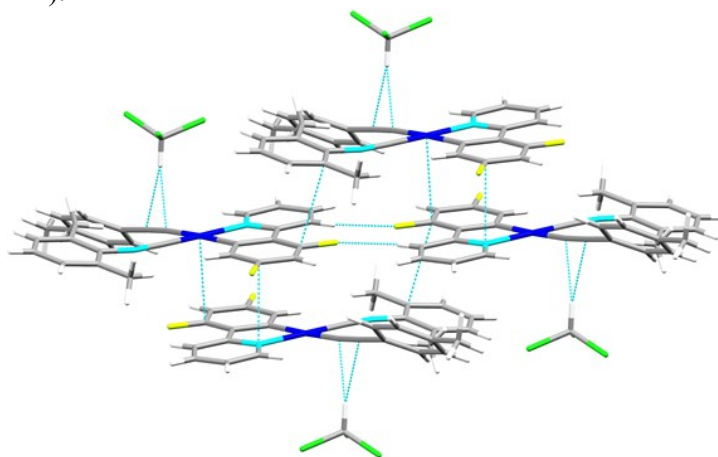


Figure S9. Crystal packing of complex **5**·CHCl₃ showing a head-to-head stacking along the *a*-axis. This organization is supported by weak $\pi \cdots \pi$ interactions (3.34 – 3.40 Å) and by secondary weak $H \cdots F$ contacts ($H \cdots F$ 2.55 Å). The crystal packing shows additional $H_{(\text{CHCl}_3)} \cdots C_{(\text{C}=\text{C})}$ (2.77 – 2.41 Å) intermolecular contacts.

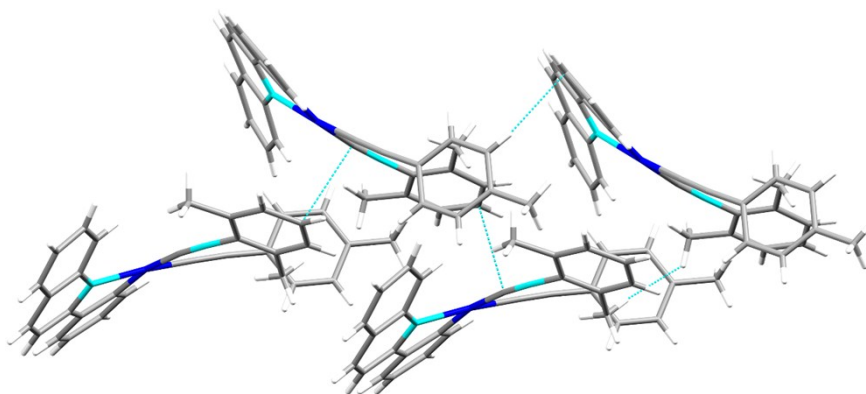


Figure S10. Crystal packing of complex **6** showing contact between $C\text{-}H_{\text{Xyl}} \cdots \text{ppy}$ 3.53 Å, $C_{\text{Xyl}} \cdots C \equiv C$ 3.28 Å and $H_{\text{Xyl}} \cdots C \equiv C$ 3.58 Å.

3.- Photophysical Properties

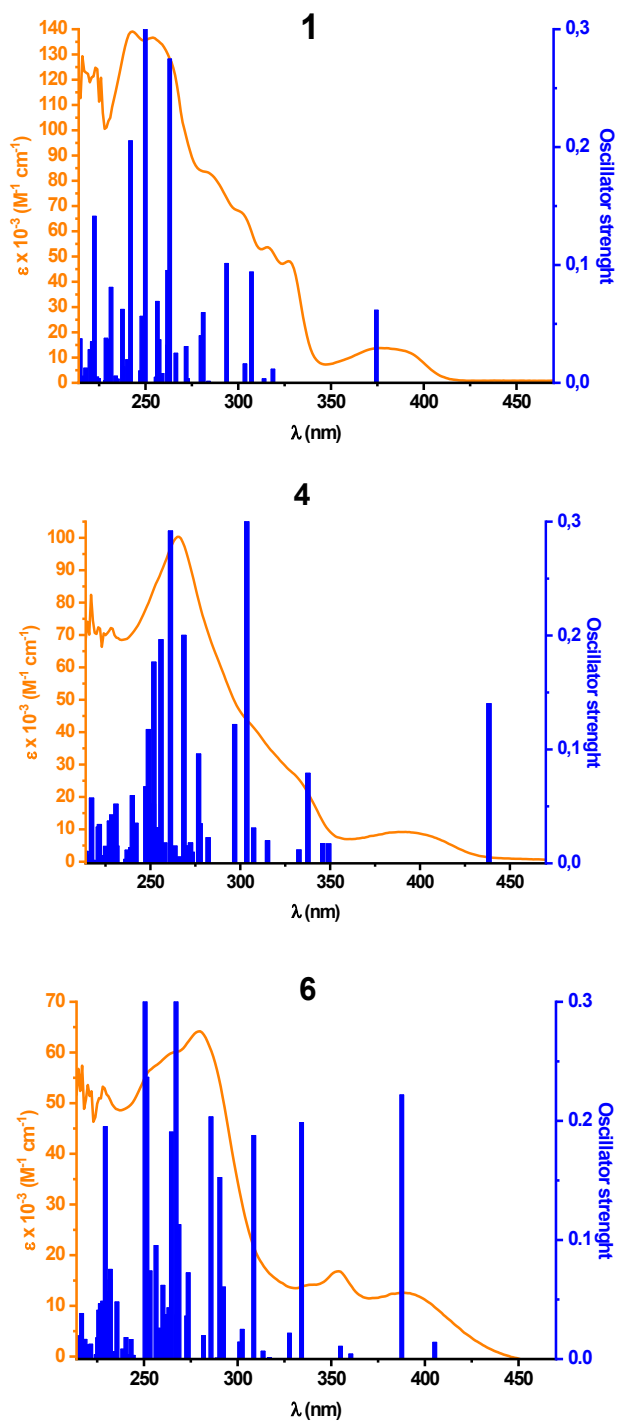
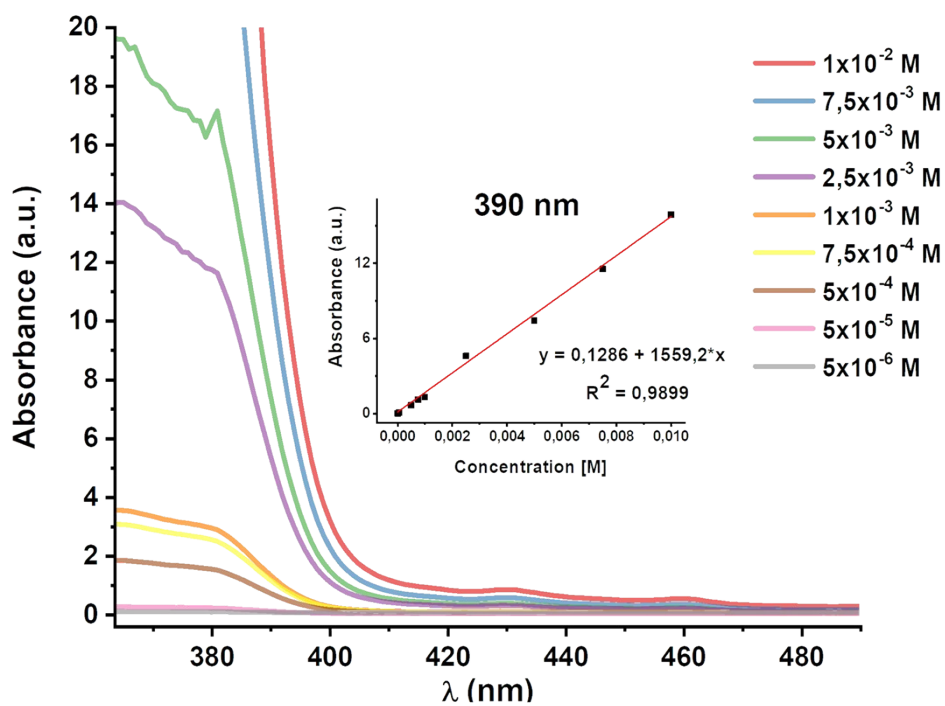
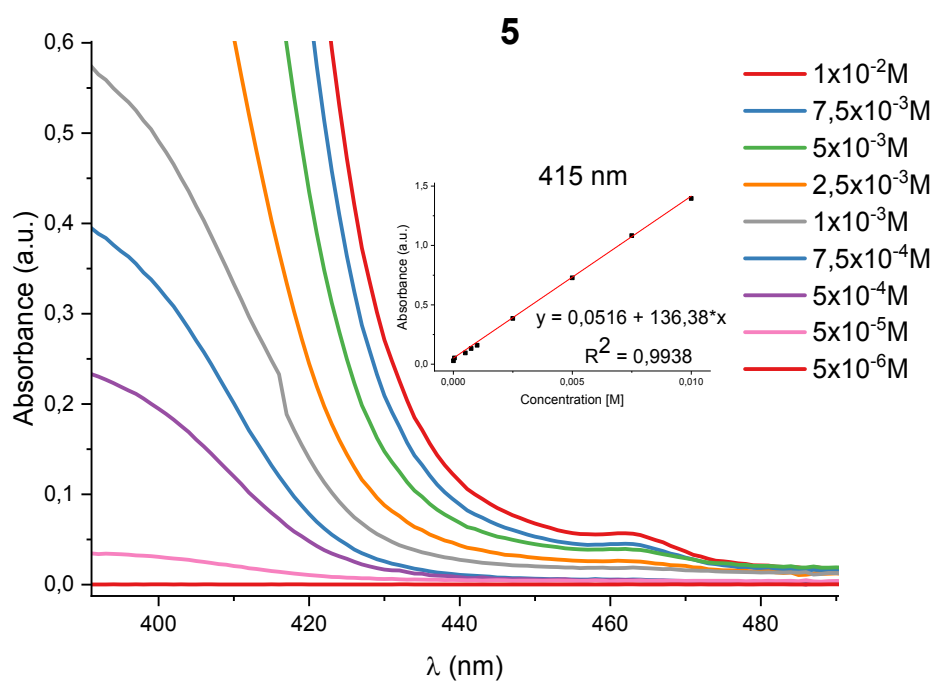


Figure S11. Calculated stick absorption spectra of **1**, **4** and **6** in CH_2Cl_2 compared with the experimental data.



a)



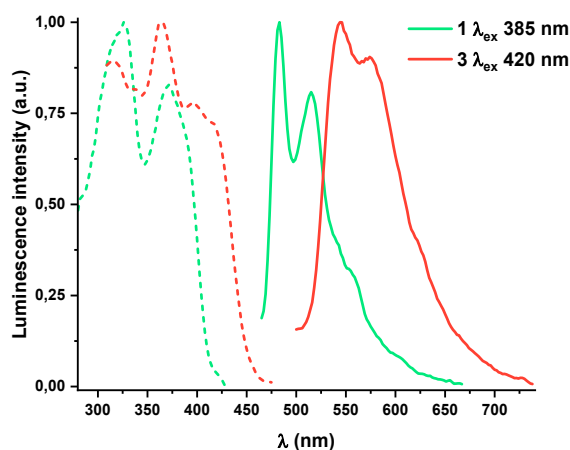
b)

Figure S12. Low-energy region of the UV-vis absorption spectra of **2** (a) and **5** (b) in CH_2Cl_2 at different concentrations. Inset: Lineal fit of the absorbance at the 390 (a) or 415 (b) nm band vs concentration.

Table S5. Photophysical data for compounds **1-6** in CH₂Cl₂ and PMMA (wt. 5%)

| Compound | Solution (5×10^{-4} M) | | | | | PMMA | |
|----------|--|--------------|------------|---|--|---|--------------|
| | 298 K | | | 77 K | | 298 K | |
| | λ_{em}/nm (λ_{ex}/nm) | $\tau/\mu s$ | ϕ (%) | λ_{em}/nm (λ_{ex}/nm) | $\tau/\mu s$ | λ_{em}/nm | ϕ (%) |
| 1 | 482, 515, 556 _{sh} (365-400) | 0.5 (482) | 0.04 | 484, 519, 554 _{max} (365-400) | 15.5 (484) 14.5 (554) | 488, 518, 552 (365-400) | 28.4 |
| 2 | <i>a</i> | <i>a</i> | <i>a</i> | 470 _{sh} , 502, 573 _{max} , 663 (385) 580, 644 (420) 680 (500) | 21.5 (470) 12.9 (573) 9.3 (680) | 476, 500, 536 _{sh} (365-400) | 24.6 |
| 3 | 545, 573 (420) | 1.4 (545) | 0.08 | 540, 582 (345- 420) | 39.7 (540) | 552, 582 (400) | 8.4 |
| 4 | 480 (365-400) | 1.3 (480) | 0.13 | 486, 519, 560 _{sh} (420) | 18.3 (486) | 486, 518, 564 _{sh} (385) | 24.0 |
| 5 | <i>a</i> | <i>a</i> | <i>a</i> | 471 _{sh} , 502, 572 _{max} , 674 _{sh} (365-420) | 14.3 (471) 14.4 (572) 12.9 (674) | 475 _{sh} , 564 (365-400) ^b 473, 500, 537 _{sh} (365- 400) | 21.3 36.4 |
| 6 | 560 (365-420) | 0.3 (560) | 0.74 | 550, 588, 650 _{sh} (365-400) | 14.3 (550) | 560, 584 (400) | 8.4 |

^a Too weak to be measured. ^b PMMA (wt. 1%)

**Figure S13.** Normalized excitation (dashed line) and emission (solid line) spectra of **1** and **3** in CH₂Cl₂ 5×10^{-4} M at 298 K.

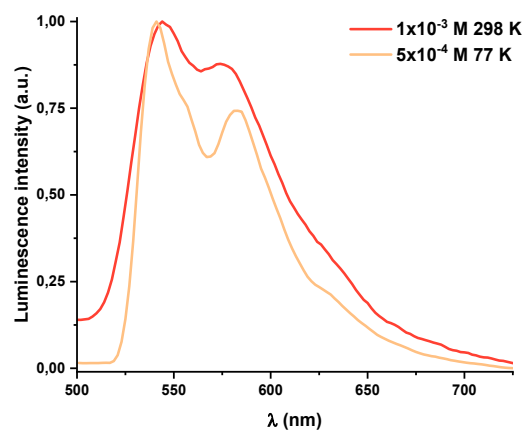


Figure S14. Normalized emission spectra of **3** in CH_2Cl_2 10^{-3} M at 298 K (red) and 5×10^{-4} M at 77 K (orange).

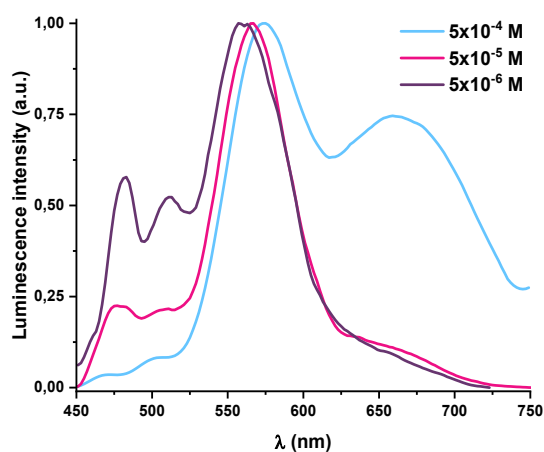


Figure S15. Normalized emission spectra of **2** in CH_2Cl_2 at different concentrations at 77 K (λ_{ex} 385 nm)

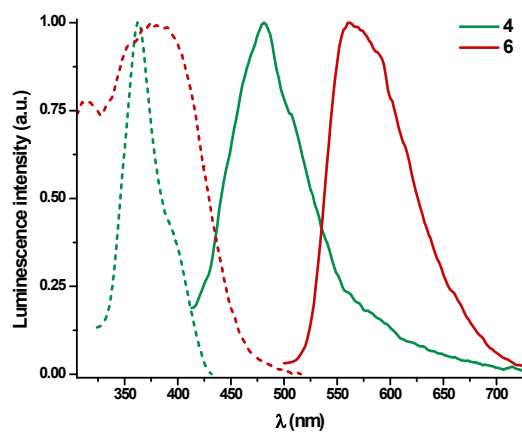


Figure S16. Normalized excitation (dashed line) and emission (solid line) spectra of **4** (λ_{ex} 385 nm) and **6** (λ_{ex} 400 nm) in CH_2Cl_2 5×10^{-4} M at 298 K.

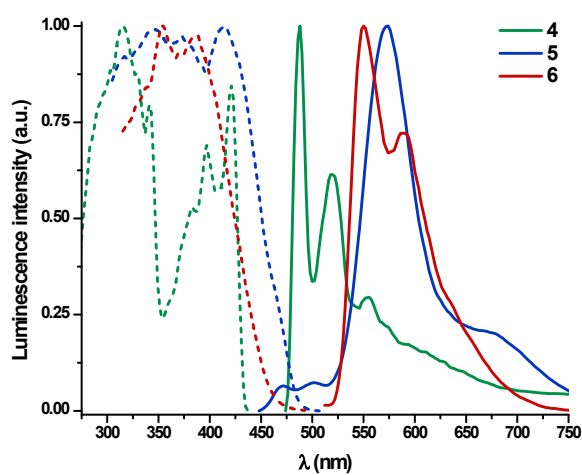


Figure S17. Normalized excitation (dashed line) and emission (solid line) spectra of **4-6** in CH_2Cl_2 5×10^{-4} M at 77 K (λ_{ex} 400 nm).

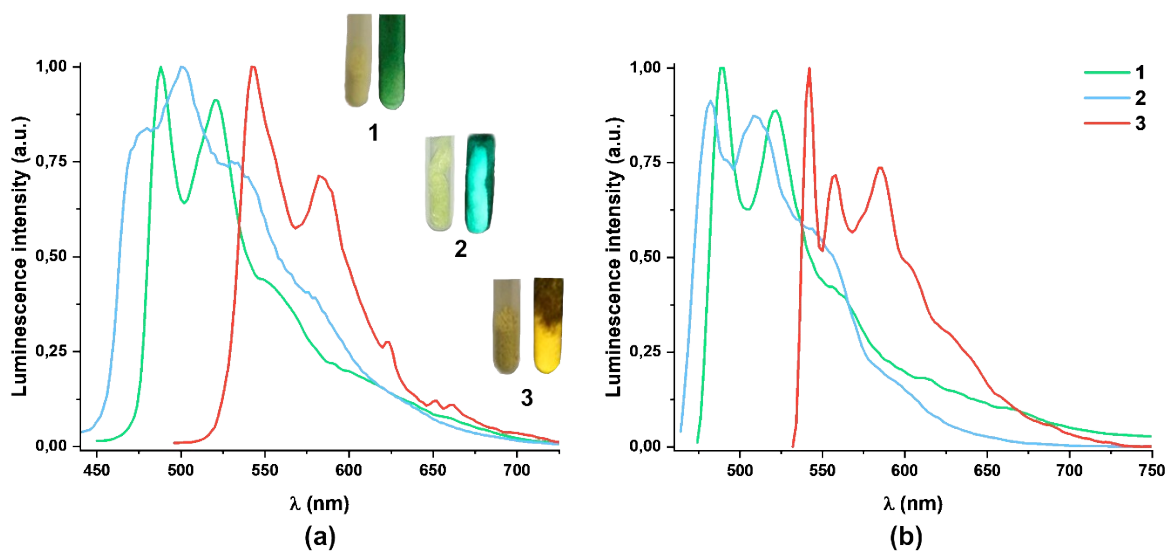


Figure S18. Normalized emission spectra of **1-3** in solid at 298 K (a) and at 77 K (b) (λ_{ex} 400 nm).

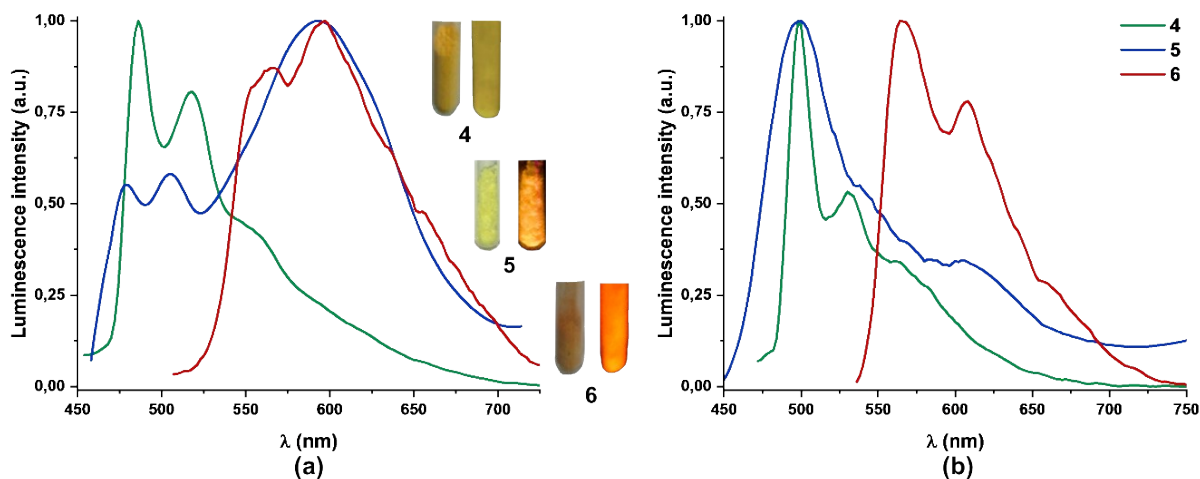


Figure S19. Normalized emission spectra of 4-6 in solid at 298 K (a) and at 77 K (b).

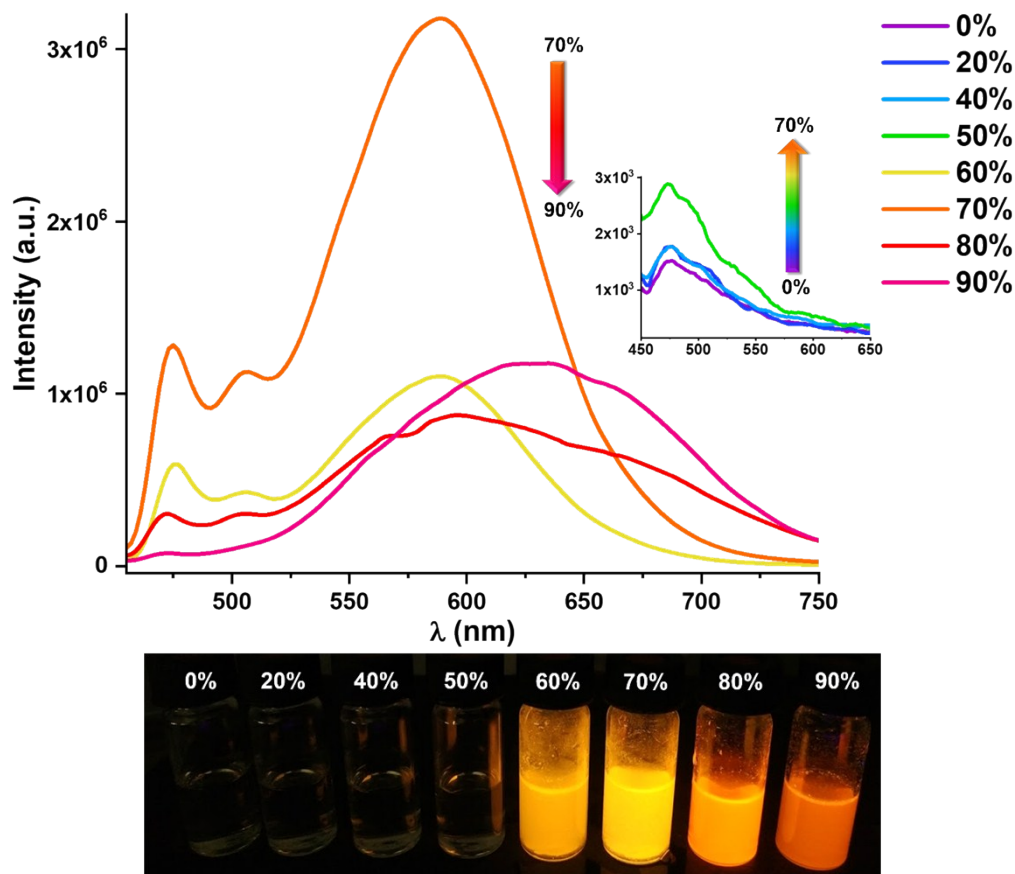


Figure S20. Emission spectra of 5 (concentration 2×10^{-4} mol L⁻¹) in THF-H₂O mixtures with different water fractions (0–90 vol%) at 298 K (λ_{ex} 385 nm). Image of the mixtures under UV illumination.

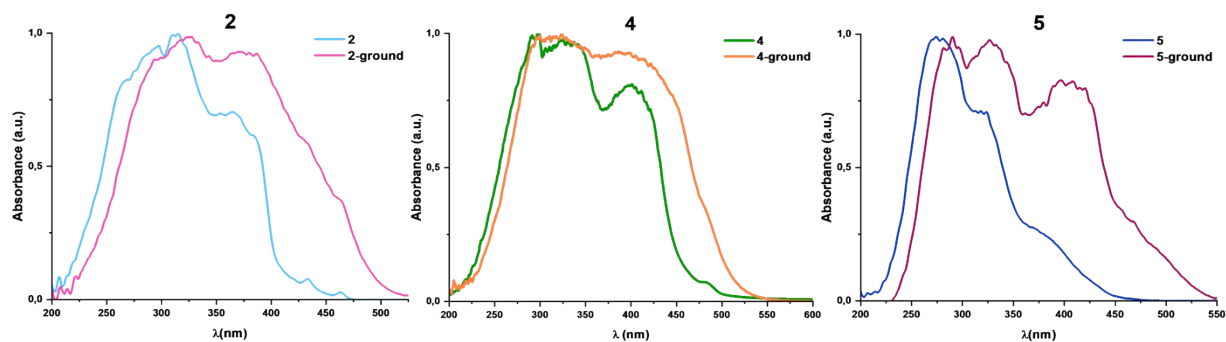


Figure S21. Normalized absorption spectra calculated from their reflectance spectra of **2**, **4** and **5** in the solid state.

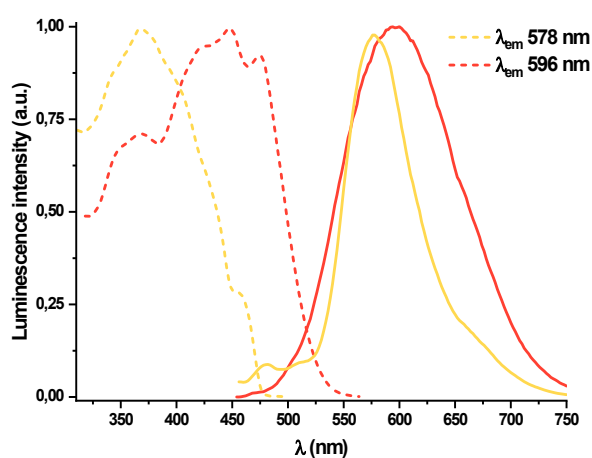


Figure S22. Normalized excitation (dashed line) and emission (solid line) spectra of **2-ground** in solid state upon mechanical grinding at 298 K (orange) and 77 K (yellow).

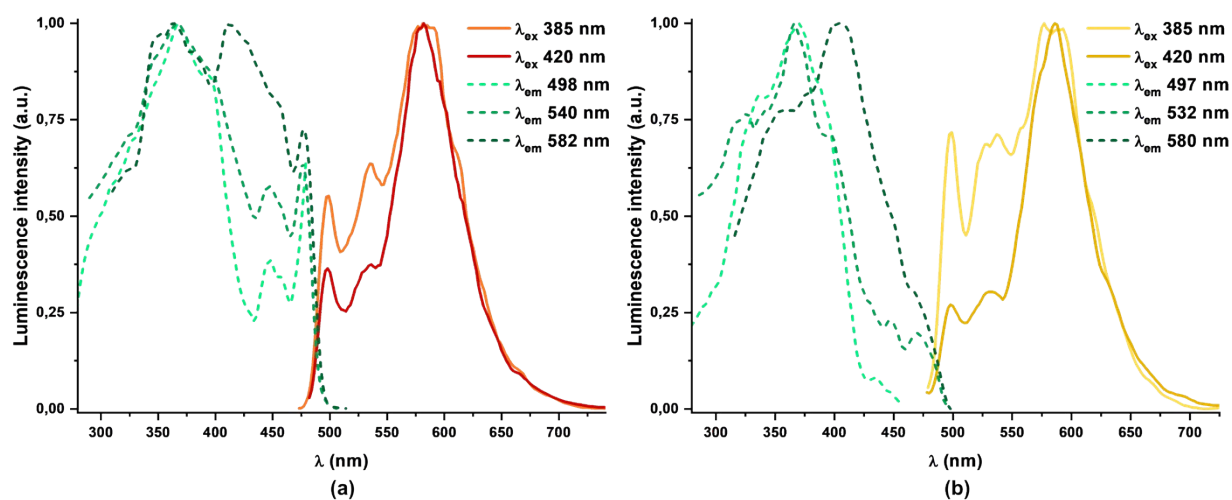


Figure S23. Normalized excitation (dashed line) and emission (solid line) spectra of **1** in solid state after grinding (a) and after 2 h (b) at 77 K.

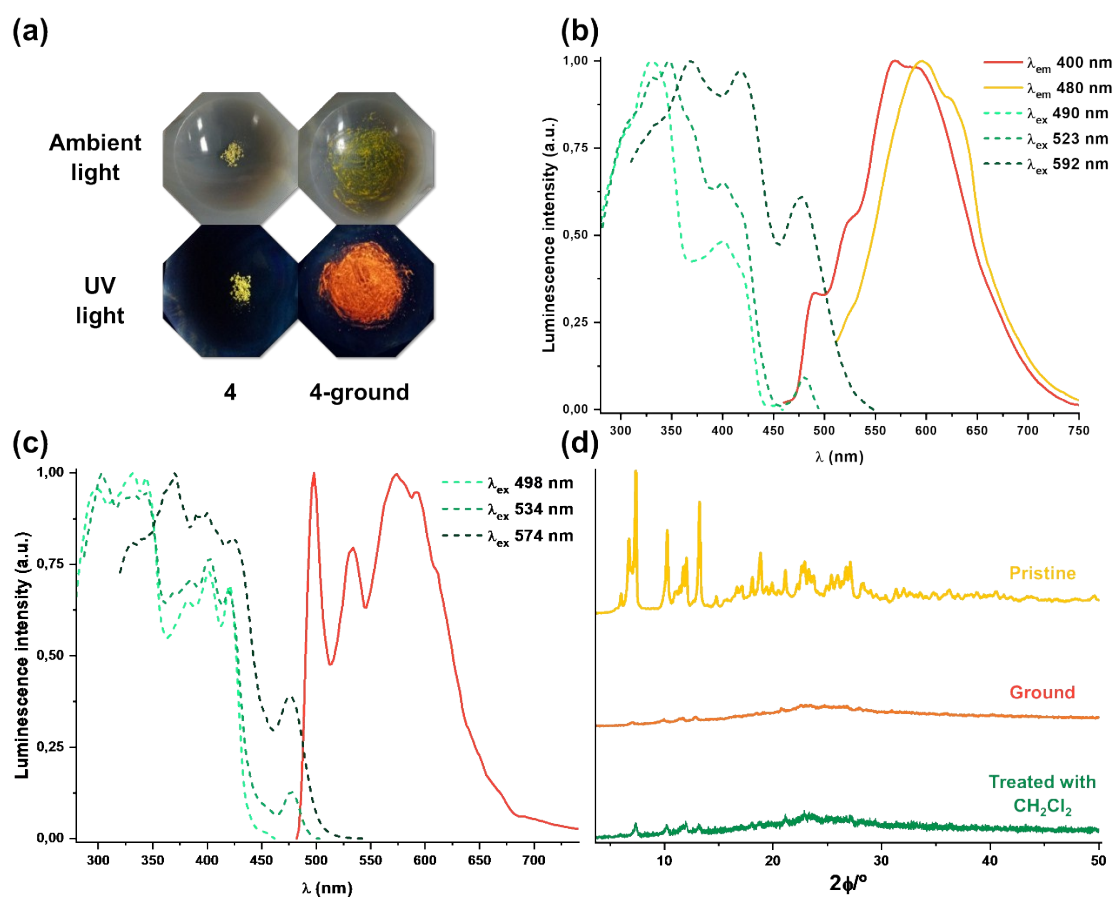


Figure S24. a) Emission colour changes of **4** by grinding. Normalized excitation and emission spectra of **4** after mechanical grinding at 298 K (b) and 77 K (c). d) XRD patterns of the pristine solid (yellow line), ground solid (orange line) and by treatment of the ground sample with a drop of CH_2Cl_2 (green line) of **4**.

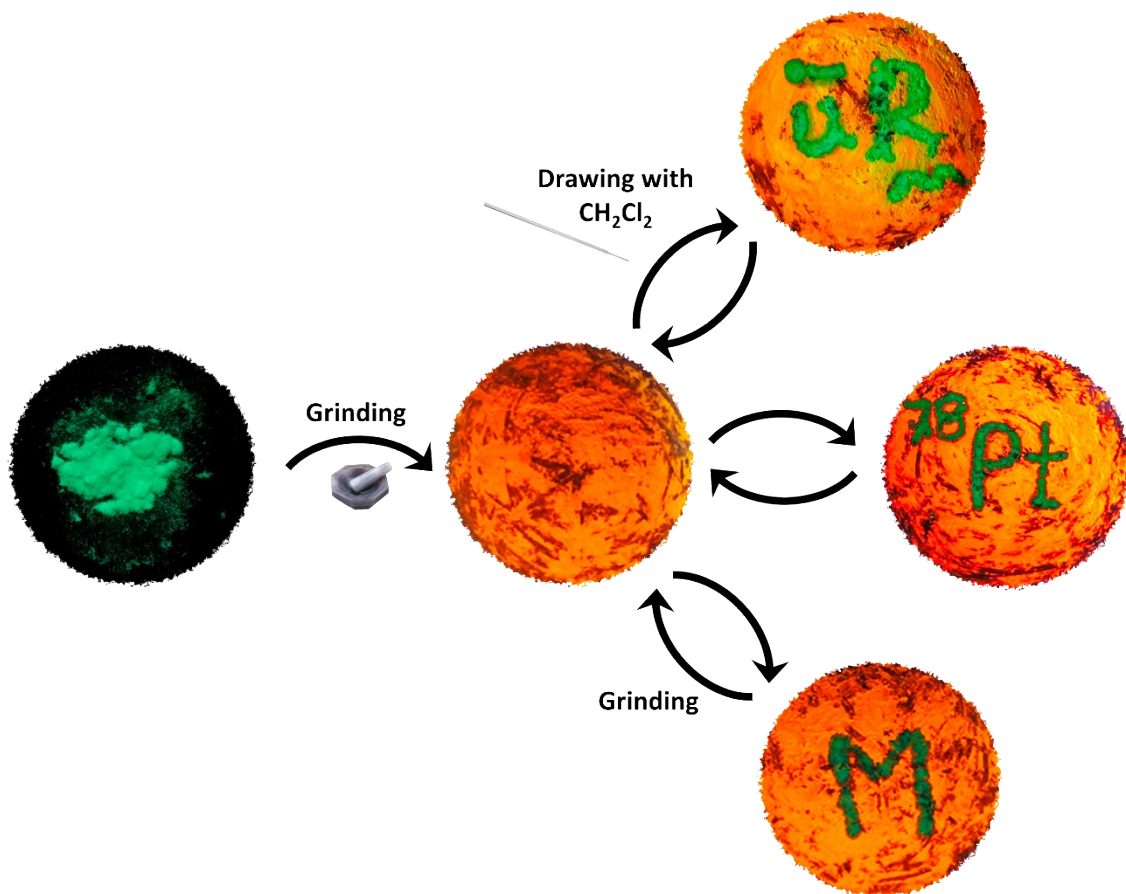


Figure S25. Photographs and schematic representation of a patterned optical recording system for **2**. Firstly, the solid was ground exhibiting an orange emission. Then, green-emitting patterns were drawn by using a glass capillary with CH₂Cl₂. The patterns were erased by mechanical grinding and the process was repeated for several times drawing.

4.- DFT and TD-DFT Calculations

The photophysical properties of complexes **1-6** were also investigated using density functional theory (DFT) and time-dependent density functional theory (TD-DFT) calculations for **1**, **4** and **6** (see Experimental for full computational details). The calculated structures and solid state structures derived from single-crystal X-ray diffraction data show good agreement (Table S6), supporting the validity of the chosen level of theory. Figures 4 and S27-29 display selected molecular orbitals (isosurface plots) and Tables S7 and S8 summarize orbital contributions and some selected low lying excited states, respectively. As displayed in Figure 4, in **1**, the highest occupied molecular orbital (HOMO) is located on the aryl ring of the ppy ligand (57%) and the Pt center (30%), whereas the HOMO-1 is mainly contributed from the ppy ligand and the lowest unoccupied orbital (LUMO) is centered on the π^* orbital of the ppy ligand. In the alkynyl-isocyanide complexes **4** and **6**, the HOMO is rather similar in both, being located on the alkynyl (73% **4**, 89% **6**) with a small contribution of the Pt center (15% **4**, 8% **6**) and the ppy in **4** (11%). The HOMO-1 and HOMO-2 is contributed of a variable composition of the cyclometalated ligand, alkynyl and platinum center. The LUMO is centered on the π^* orbital of the C^N ligand (73% **4**, 91% **6**), whereas in the LUMO+1 has mainly located on the CNR ligand. For **1**, the lowest S₁ state (374.42 nm) is contributed by HOMO to LUMO transitions, supporting a mixed intraligand/metal-to-ligand (¹IL/¹MLCT) character. The red shift observed experimentally from **1** to **4** is in accordance with the calculations (S₁ state calculated 438.34 nm **4** vs 374.42 nm **1**) and it is consequence of a notable destabilization of the HOMO, now located on the alkynyl donor group. In **4**, the lowest calculated singlet has a configuration HOMO→LUMO (98%) and a mainly ligand-to-ligand charge transfer (¹L'LCT, C≡CtoI→ppy). The blue shift observed experimentally in **6** in relation to its precursor **3** is explained by the calculations because the most intense calculated transition is now S₃ (387.68 nm), which correspond to a mixed [HOMO-2→LUMO (83%), HOMO-1→LUMO (15%)], having intraligand (pq), metal-to-ligand (pq) and alkynyl-to-pq character ¹IL/¹MLCT/¹L'LCT. As noted before, the S₁ (HOMO→LUMO) with alkynyl-to-pq character (¹L'LCT) calculated at 455 nm has negligible intensity.

The lowest-lying (S₀→T₁, Table S8) and spin density distribution of the triplet excited states (T₁, Figure 6) based on their corresponding optimized S₀ and T₁ geometries, respectively have been also calculated. For complex **1**, the S₀→T₁ transition mainly results from a mixing of IL (ppy) and Pt→ppy excitations with some Cl-to-ppy contribution. The calculated spin-density distribution in the optimized T₁ state (Pt, 0.1735), as well as the SOMO and SOMO-1 orbitals (Table S9, Figure S30) are located on the ppy and Pt, with a low contribution of Cl, supporting a mixture ³IL/³MLCT with negligible ³XLCT contribution. In the alkynyl-isocyanide ppy

complex **4**, the C≡CTol and the ppy cyclometalated group contribute to S₀→T₁ (HOMO→LUMO 77%) transition. Therefore, the alkynyl to cyclometalated charge transfer ³L'LCT [with very low ³IL/³MLCT/³ML''CT (L'' = CNXyl) contribution] account for the excitation, in agreement with the absorption features. The spin density in the optimized T₁ state (Pt 0.248) as well as the SOMO and SOMO-1 orbitals are located on the C^N (ppy) ligand, the C≡CTol, the Pt and a minor extent on the CNXyl, being the emission ³IL/³L'LCT/³MLCT in nature with minor ³ML''CT contribution. In the pq complex **6**, the calculations indicated that the S₀→T₁ transition result from a mixture of C≡CTol→pq, Pt→pq and IL (pq) excitations. The spin density in the optimized T₁ state (Pt 0.235) and the SOMO and SOMO-1 orbitals supports a mixed ³IL/³L'LCT/³MLCT nature for the phosphorescent emission. The change from a *trans-C, CNXyl* in **4** to a *cis-N, CNXyl* in **6** is reflected in a lower contribution of the isocyanide in the emissive state (see Table S9). As was expected, the contribution of the Pt atom to the SOMOs is higher in both alkynyl complexes (**4**, **6**) than in the chloride derivative **1** in agreement with the higher values of quantum yield in solution for the alkynyl series. The calculated energy emission (Figure 6) gives values consistent with the trend observed for the experimental phosphorescence in fluid solution as well as in rigid media.

Table S6. DFT optimized geometries for ground state and triplet state of **1**, **4**, and **6** in CH₂Cl₂.

| 1 | | | |
|------------------|------------|----------------|----------------|
| | X-ray | S ₀ | T ₁ |
| Pt(1)-N(2) | 2.063(3) | 2.1010 | 2.0636 |
| Pt(1)-C(10) | 1.986(4) | 2.0141 | 1.9753 |
| Pt(1)-C(1) | 1.901(4) | 1.9108 | 1.9263 |
| Pt(1)-Cl(1) | 2.3901(10) | 2.5163 | 2.5129 |
| N(1)-C(1) | 1.153(5) | 1.1710 | 1.1713 |
| N(1)-C(2) | 1.399(5) | 1.3867 | 1.3860 |
| C(10)-Pt(1)-N(2) | 80.62(15) | 80.37 | 81.65 |
| C(1)-Pt(1)-Cl(1) | 89.43(12) | 89.05 | 87.32 |
| N(2)-Pt(1)-Cl(1) | 94.55(10) | 94.70 | 94.45 |
| C(1)-Pt(1)-C(10) | 95.47(17) | 95.91 | 96.58 |

| 4 | | | |
|------------------|-----------|----------------|----------------|
| | X-ray | S ₀ | T ₁ |
| Pt(1)-N(2) | 2.049(5) | 2.110 | 2.074 |
| Pt(1)-C(10) | 2.049(5) | 2.062 | 2.013 |
| Pt(1)-C(1) | 1.933(6) | 1.900 | 1.920 |
| Pt(1)-C(21) | 2.087(7) | 2.054 | 2.033 |
| N(1)-C(1) | 1.156(7) | 1.172 | 1.174 |
| C(21)-C(22) | 1.058(8) | 1.229 | 1.237 |
| N(2)-Pt(1)-C(10) | 80.58(19) | 79.63 | 80.88 |
| C(1)-Pt(1)-C(21) | 89.1(2) | 90.72 | 89.73 |
| N(2)-Pt(1)-C(21) | 93.4(2) | 94.12 | 93.75 |
| C(1)-Pt(1)-C(10) | 97.1(2) | 95.54 | 95.66 |

| 6 | | | |
|----------------|------------|----------------|----------------|
| | X-ray | S ₀ | T ₁ |
| Pt(1) - N(1) | 2.102(3) | 2.184 | 2.061 |
| Pt(1) - C(1) | 2.016(4) | 2.037 | 2.037 |
| Pt(1) - C(16) | 1.960(4) | 2.017 | 2.039 |
| Pt(1) - C(25) | 1.977(4) | 1.968 | 1.957 |
| N(2)-C(16) | 1.178(5) | 1.173 | 1.172 |
| C(25)-C(26) | 1.186(5) | 1.226 | 1.234 |
| C(1)-Pt-N(1) | 79.92(14) | 79.23 | 80.74 |
| C(16)-Pt-C(25) | 84.39(15) | 85.34 | 86.98 |
| C(16)-Pt-N(1) | 101.57(13) | 102.92 | 99.80 |
| C(25)-Pt-C(1) | 93.62(15) | 92.30 | 92.55 |

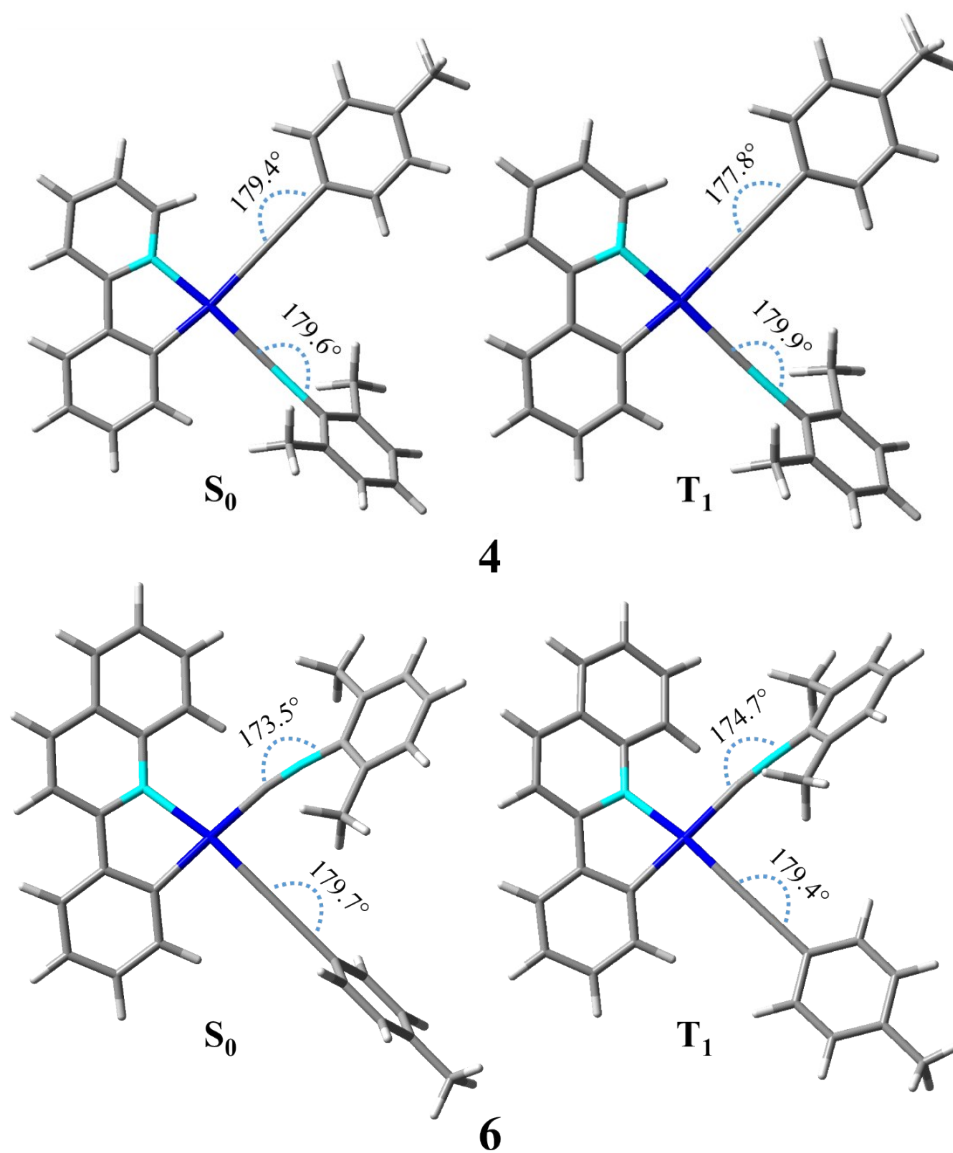


Figure S26. Optimized geometries by DFT calculations for **4** and **6** in S_0 and T_1 , including the $CNXYl$ and $C\equiv CTol$ angles.

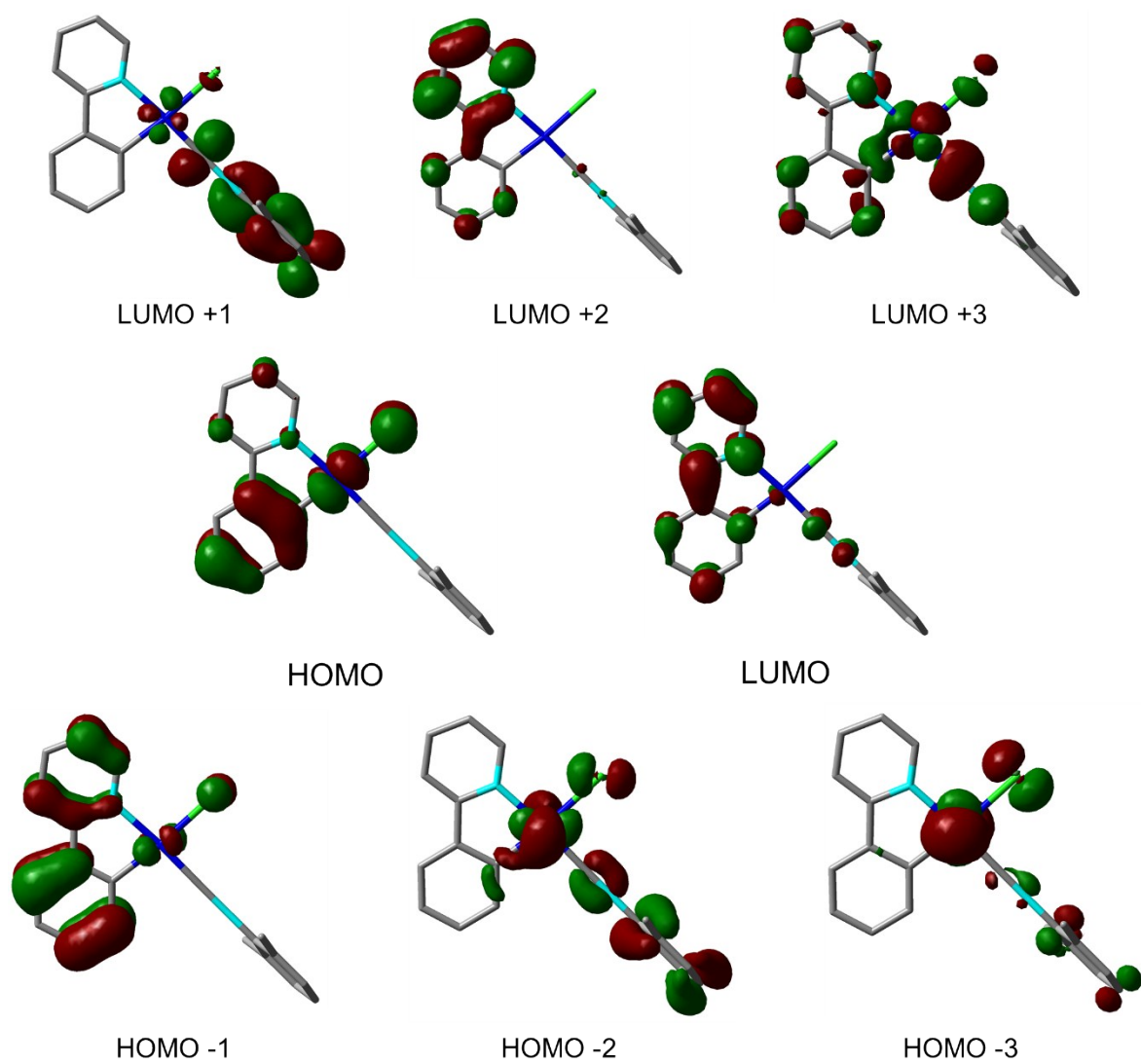


Figure S27. Selected frontier Molecular Orbitals for **1** in the ground state.

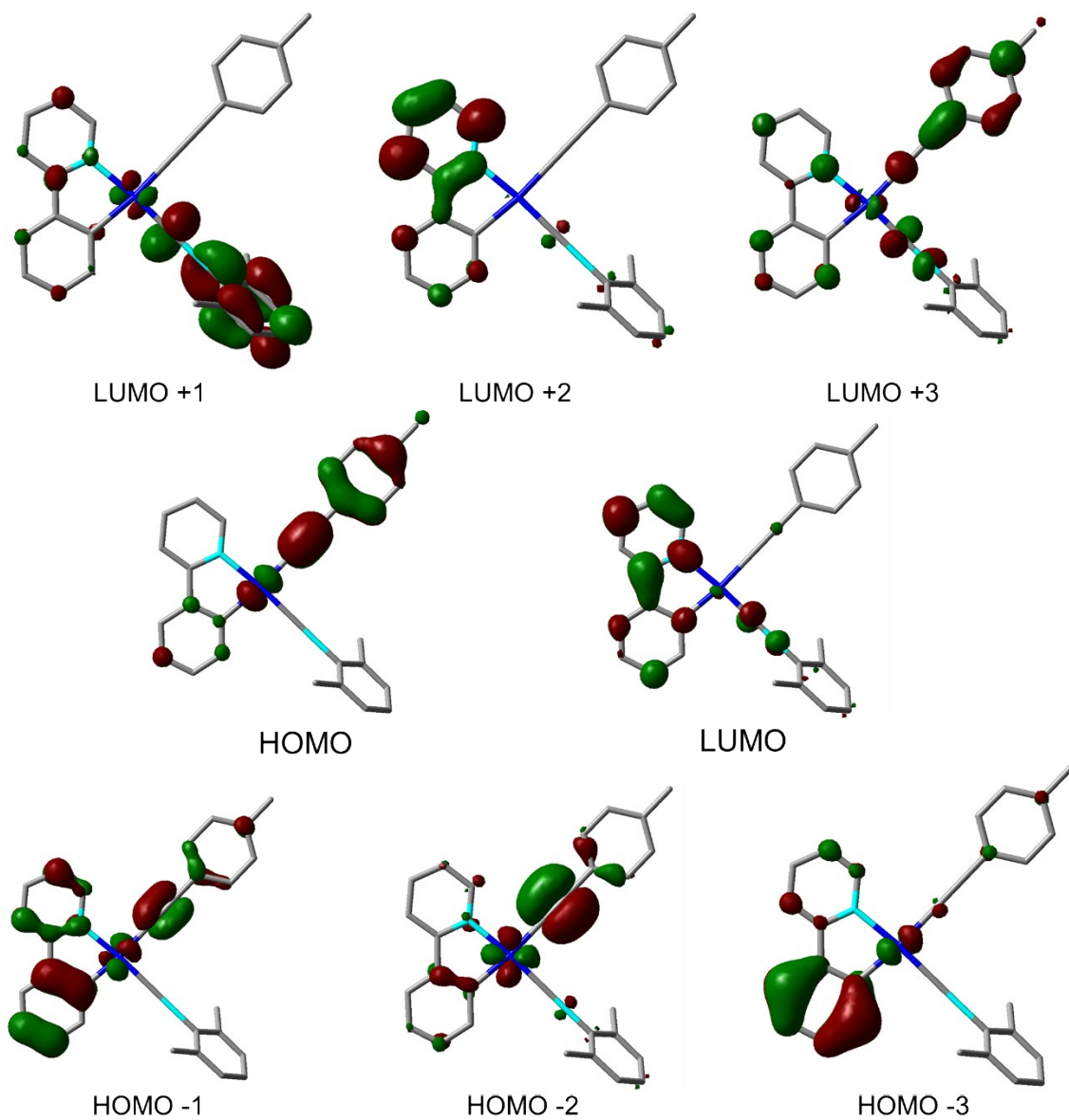


Figure S28. Selected frontier Molecular Orbitals for **4** in the ground state.

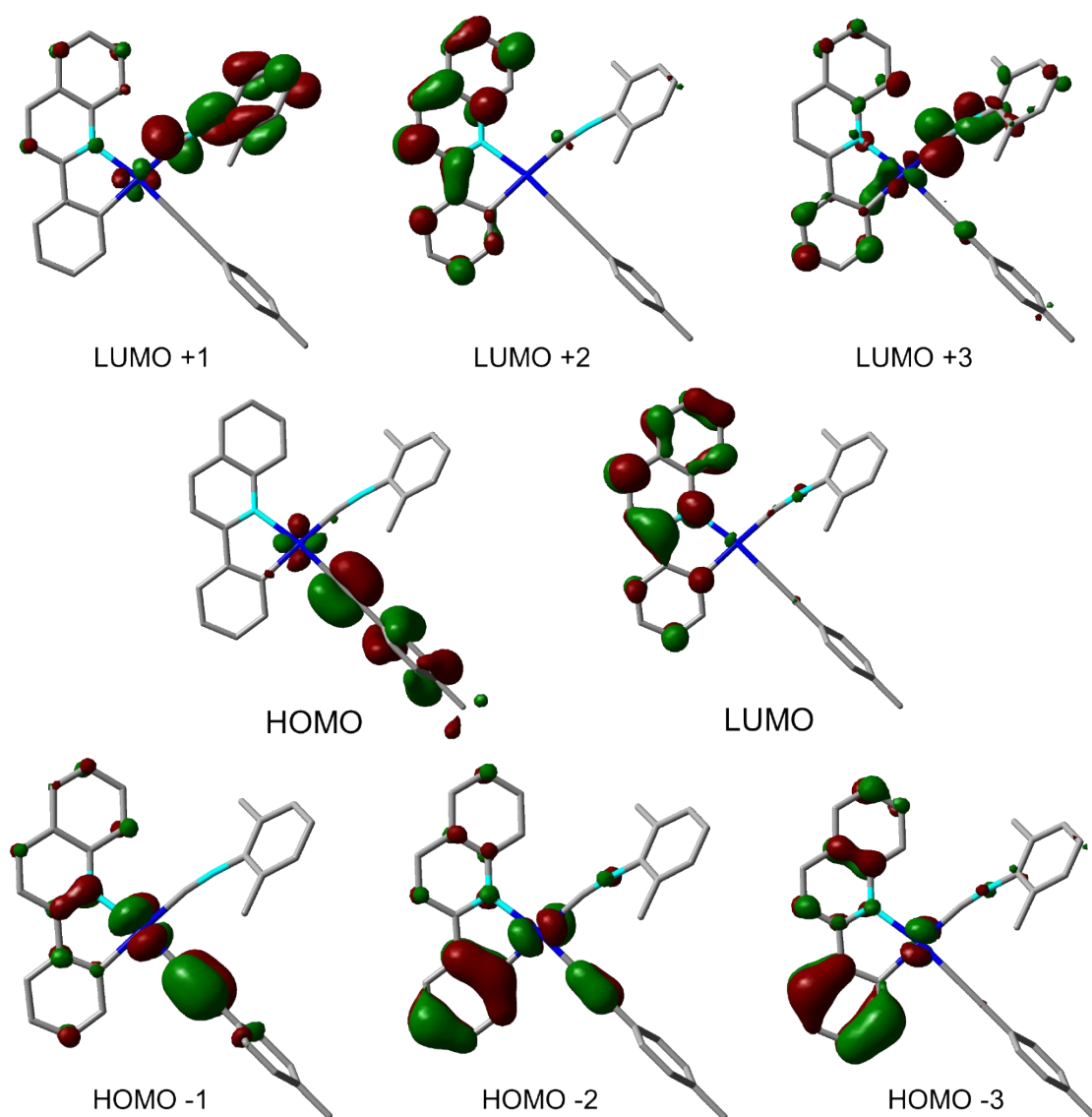


Figure S29. Selected frontier Molecular Orbitals for **6** in the ground state.

Table S7. Composition (%) of Frontier MOs in terms of ligands and metals in the ground state for **1**, **4** and **6** in CH₂Cl₂.

| 1 | | | | | |
|----------|-------|-----|----|----|-------|
| MO | eV | ppy | Cl | Pt | CNXyl |
| LUMO+5 | -0.28 | 0 | 0 | 0 | 100 |
| LUMO+4 | -0.42 | 35 | 5 | 40 | 20 |
| LUMO+3 | -0.51 | 35 | 3 | 35 | 28 |
| LUMO+2 | -1.14 | 96 | 0 | 1 | 3 |
| LUMO+1 | -1.35 | 4 | 2 | 7 | 88 |
| LUMO | -1.96 | 83 | 0 | 8 | 8 |
| HOMO | -6.01 | 57 | 13 | 30 | 0 |
| HOMO-1 | -6.6 | 87 | 6 | 6 | 1 |
| HOMO-2 | -6.69 | 7 | 8 | 39 | 46 |
| HOMO-3 | -6.75 | 4 | 13 | 67 | 15 |
| HOMO-4 | -6.91 | 0 | 0 | 0 | 100 |
| HOMO-5 | -7.0 | 3 | 64 | 9 | 24 |

| 4 | | | | | |
|----------|-------|-----|-----|----|-------|
| MO | eV | ppy | C≡C | Pt | CNXyl |
| LUMO+5 | -0.03 | 10 | 51 | 13 | 26 |
| LUMO+4 | -0.25 | 0 | 0 | 0 | 100 |
| LUMO+3 | -0.67 | 23 | 43 | 19 | 15 |
| LUMO+2 | -1.02 | 92 | 0 | 1 | 7 |
| LUMO+1 | -1.21 | 17 | 0 | 4 | 78 |
| LUMO | -1.91 | 73 | 4 | 10 | 13 |
| HOMO | -5.32 | 11 | 73 | 15 | 0 |
| HOMO-1 | -6.18 | 66 | 26 | 8 | 1 |
| HOMO-2 | -6.24 | 15 | 66 | 14 | 5 |
| HOMO-3 | -6.55 | 82 | 9 | 7 | 2 |
| HOMO-4 | -6.64 | 15 | 7 | 36 | 42 |
| HOMO-5 | -6.74 | 2 | 5 | 66 | 27 |

| 6 | | | | | |
|----------|-------|----|-----|----|-------|
| MO | eV | pq | C≡C | Pt | CNXyl |
| LUMO+5 | -0.26 | 0 | 0 | 0 | 99 |
| LUMO+4 | -0.32 | 4 | 91 | 3 | 2 |
| LUMO+3 | -0.64 | 29 | 7 | 23 | 41 |
| LUMO+2 | -1.07 | 94 | 0 | 1 | 5 |
| LUMO+1 | -1.41 | 14 | 1 | 9 | 76 |
| LUMO | -2.19 | 91 | 1 | 4 | 3 |
| HOMO | -5.43 | 2 | 89 | 8 | 1 |
| HOMO-1 | -5.89 | 24 | 42 | 33 | 1 |
| HOMO-2 | -6.00 | 63 | 13 | 20 | 5 |
| HOMO-3 | -6.46 | 83 | 3 | 9 | 6 |
| HOMO-4 | -6.49 | 9 | 3 | 88 | 1 |
| HOMO-5 | -6.73 | 0 | 99 | 0 | 1 |

Table S8. Selected vertical excitation energies singlets (S_0) and the first triplet computed by TDDFT/SCRf (CH_2Cl_2) with the orbitals involved for **1**, **4** and **6**.

| 1 | | | | |
|-----------------|-----------------|---------------------|--|--|
| | State | λ/nm | f | Transition (% Contribution) |
| 1 | T ₁ | 451.0 | - | H-1→LUMO (15%), HOMO→LUMO (70%) |
| | T ₂ | 370.5 | - | H-1→LUMO (54%), H-1→L+2 (10%), HOMO→LUMO (25%) |
| | T ₃ | 370.3 | - | H-5→L+1 (14%), H-4→L+5 (17%), H-3→L+1 (13%), H-2→L+1 (45%) |
| | S ₁ | 374.42 | 0,0616 | HOMO→LUMO (98%) |
| | S ₂ | 318.70 | 0,0116 | H-3→LUMO (51%), H-2→LUMO (39%) |
| | S ₃ | 313.93 | 0,0034 | HOMO→L+1 (82%) |
| | S ₄ | 307.15 | 0,094 | H-1→LUMO (75%), HOMO→L+2 (16%) |
| | S ₅ | 303.62 | 0,0161 | H-3→LUMO (39%), H-2→LUMO (45%) |
| | S ₆ | 293.74 | 0,1013 | H-1→LUMO (16%), HOMO→L+2 (68%) |
| | S ₇ | 283.94 | 0,0013 | HOMO→L+3 (31%), HOMO→L+4 (52%) |
| | S ₈ | 281.11 | 0,0596 | H-5→LUMO (82%) |
| | S ₉ | 279.95 | 0,0399 | H-3→L+1 (42%), H-2→L+1 (28%) |
| | S ₁₀ | 272.70 | 0,0035 | H-4→LUMO (96%) |
| S ₁₁ | 271.89 | 0,0308 | H-6→LUMO (83%) | |
| S ₁₂ | 266.42 | 0,0251 | H-7→LUMO (28%), HOMO→L+3 (21%), HOMO→L+4 (12%) | |
| | State | λ/nm | f | Transition (% Contribution) |
| 4 | T ₁ | 486.67 | - | HOMO→LUMO (77%) |
| | T ₂ | 427.93 | - | H-1→LUMO (44%), HOMO→L+3 (12%) |
| | T ₃ | 389.87 | - | HOMO→LUMO (14%), HOMO→L+3 (39%), HOMO→L+5 (14%) |
| | S ₁ | 438.34 | 0.1402 | HOMO→LUMO (98%) |
| | S ₂ | 349.19 | 0.0171 | HOMO→L+1 (98%) |
| | S ₃ | 345.88 | 0.0174 | H-2→LUMO (62%), H-1→LUMO (36%) |
| | S ₄ | 337.62 | 0.0791 | H-2→LUMO (35%), H-1→LUMO (60%) |
| | S ₅ | 332.61 | 0.0118 | HOMO→L+2 (97%) |
| | S ₆ | 315.16 | 0.0199 | H-5→LUMO (41%), H-4→LUMO (56%) |
| | S ₇ | 307.41 | 0.031 | H-3→LUMO (65%), HOMO→L+3 (26%) |
| | S ₈ | 303.61 | 0.6162 | H-3→LUMO (23%), HOMO→L+3 (67%) |
| | S ₉ | 282.11 | 0.1219 | H-5→LUMO (52%), H-4→LUMO (37%) |
| | S ₁₀ | 279.99 | 0.0225 | H-2→L+1 (59%), H-1→L+1 (32%) |
| S ₁₁ | 277.67 | 0.0002 | H-6→LUMO (89%) | |
| S ₁₂ | 276.80 | 0.0348 | H-8→LUMO (68%), H-1→L+1 (16%) | |
| 6 | T ₁ | 510.28 | - | H-6→LUMO (11%), H-2→LUMO (17%), H-1→LUMO (54%) |
| | T ₂ | 457.96 | - | HOMO→LUMO (94%) |
| | T ₃ | 437.30 | - | H-6→LUMO (15%), H-2→LUMO (64%) |
| | S ₁ | 455.35 | 0.0010 | HOMO→LUMO (98%) |
| | S ₂ | 405.29 | 0.0140 | H-2→LUMO (15%), H-1→LUMO (82%) |

| | | | |
|-----------------|--------|--------|--------------------------------|
| S ₃ | 387.68 | 0.2218 | H-2→LUMO (83%), H-1→LUMO (15%) |
| S ₄ | 360.46 | 0.0042 | HOMO→L+1 (95%) |
| S ₅ | 354.93 | 0.0107 | H-4→LUMO (95%) |
| S ₆ | 334.16 | 0.1986 | H-3→LUMO (87%) |
| S ₇ | 327.69 | 0.0217 | H-1→L+1 (93%) |
| S ₈ | 316.98 | 0.0012 | HOMO→L+2 (92%) |
| S ₉ | 313.57 | 0.0066 | H-6→LUMO (62%), H-2→L+1 (18%) |
| S ₁₀ | 308.62 | 0.1877 | H-6→LUMO (19%), H-2→L+1 (70%) |
| S ₁₁ | 302.47 | 0.0249 | H-7→LUMO (57%), HOMO→L+3 (33%) |
| S ₁₂ | 301.14 | 0.0142 | H-7→LUMO (34%), HOMO→L+3 (59%) |

Table S9. Composition (%) of Frontier MOs in terms of ligands and metals in the first triplet state for **1**, **4** and **6** in CH₂Cl₂.

| 1 | | | | | |
|----------|-------|-----|----|----|-------|
| MO | eV | ppy | Cl | Pt | CNXyl |
| SOMO | -3.56 | 90 | 1 | 6 | 1 |
| SOMO-1 | -4.52 | 86 | 2 | 12 | 0 |

| 4 | | | | | |
|----------|-------|-----|-----|----|-------|
| MO | eV | ppy | C≡C | Pt | CNXyl |
| SOMO | -3.13 | 82 | 3 | 8 | 6 |
| SOMO-1 | -4.42 | 59 | 25 | 17 | 0 |

| 6 | | | | | |
|----------|-------|----|-----|----|-------|
| MO | eV | pq | C≡C | Pt | CNXyl |
| SOMO | -3.61 | 93 | 2 | 4 | 2 |
| SOMO-1 | -4.39 | 53 | 26 | 20 | 1 |

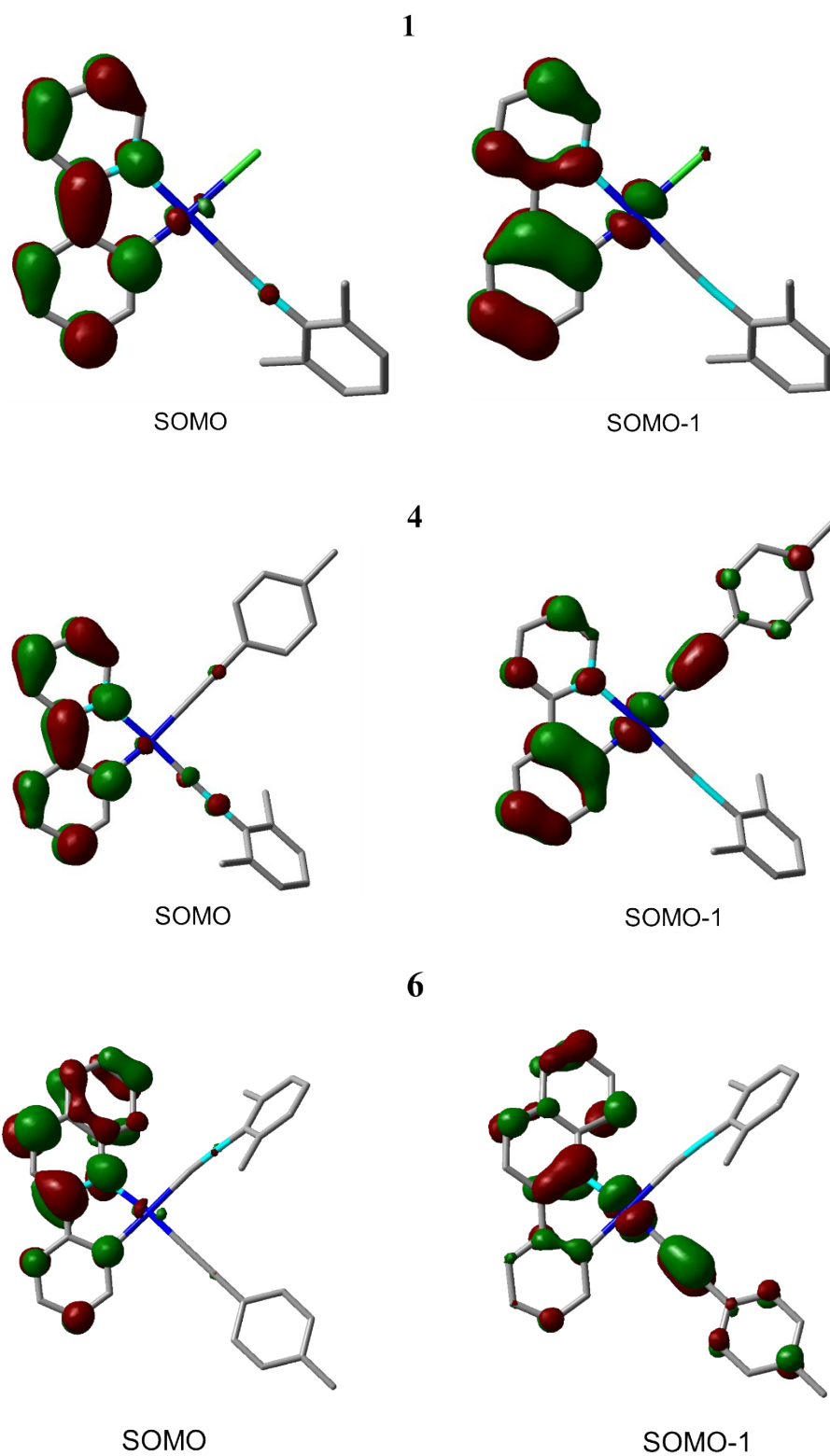


Figure S30. Frontier orbitals plots obtained by DFT for the first triplet state of **1**, **4** and **6**.

Complete References:

(30) Frisch, M. J.; Trucks, G. W.; Schlegel, H. B.; Scuseria, G. E.; Robb, M. A.; Cheeseman, J. R.; Scalmani, G.; Barone, V.; Mennucci, B.; Petersson, G. A.; Nakatsuji, H.; Caricato, M.; Li, X.; Hratchian, H. P.; Izmaylov, A. F.; Bloino, J.; Zheng, G.; Sonnenberg, J. L.; Hada, M.; Ehara, M.; Toyota, K.; Fukuda, R.; Hasegawa, J.; Ishida, M.; Nakajima, T.; Honda, Y.; Kitao, O.; Nakai, H.; Vreven, T.; Montgomery, J. A.; Peralta, J. E.; Ogliaro, F.; Bearpark, M.; Heyd, J. J.; Brothers, E.; Kudin, K. N.; Staroverov, V. N.; Kobayashi, R.; Normand, J.; Raghavachari, K.; Rendell, A.; Burant, J. C.; Iyengar, S. S.; Tomasi, J.; Cossi, M.; Rega, N.; Millam, J. M.; Klene, M.; Knox, J. E.; Cross, J. B.; Bakken, V.; Adamo, C.; Jaramillo, J.; Gomperts, R.; Stratmann, R. E.; Yazyev, O.; Austin, A. J.; Cammi, R.; Pomelli, C.; Ochterski, J. W.; Martin, R. L.; Morokuma, K.; Zakrzewski, V. G.; Voth, G. A.; Salvador, P.; Dannenberg, J. J.; Dapprich, S.; Daniels, A. D.; Farkas, J. B.; Foresman, J. B.; Ortiz, J. V.; Cioslowski, J.; Fox, D. J. *Gaussian 09, Revision B.01* Gaussian, Inc., Wallingford CT, , 2009.

(31) Frisch M. J.; Trucks, G. W.; Schlegel, H. B.; Scuseria, G. E.; Robb, M. A.; Cheeseman, J. R.; Scalmani, G.; Barone, V.; Petersson, G. A.; Nakatsuji, H.; Li, X.; Caricato, M.; Marenich, A. V.; Bloino, J.; Janesko, B. G.; Gomperts, R.; Mennucci, B.; Hratchian, H. P.; Ortiz, J. V.; Izmaylov, A. F.; Sonnenberg, J. L.; Williams-Young, D.; Ding, F.; Lipparini, F.; Egidi, F.; Goings, J.; Peng, B.; Petrone, A.; Henderson, T.; Ranasinghe, D.; Zakrzewski, V. G.; Gao, J.; Rega, N.; Zheng, G.; Liang, W.; Hada, M.; Ehara, M.; Toyota, K.; Fukuda, R.; Hasegawa, J.; Ishida, M.; Nakajima, T.; Honda, Y.; Kitao, O.; Nakai, H.; Vreven, T.; Throssell, K.; Montgomery, Jr. J. A.; Peralta, J. E.; Ogliaro, F.; Bearpark, M. J.; Heyd, J. J.; Brothers, E. N.; Kudin, K. N.; Staroverov, V. N.; Keith, T. A.; Kobayashi, R.; Normand, J.; Raghavachari, K.; Rendell, A. P.; Burant, J. C.; Iyengar, S. S.; Tomasi, J.; Cossi, M.; Millam, J. M.; Klene, M.; Adamo, C.; Cammi, R.; Ochterski, J. W.; Martin, R. L.; Morokuma, K.; Farkas, O.; Foresman, J. B.; and Fox D. J., *Revision A.03, Inc., Gaussian 16* Wallingford CT, 2016, 2016.